https://doi.org/10.1016/j.ijheatmasstransfer.2021.122199

A proposed paper submitted to

International Journal of Heat and Mass Transfer

Heat Transfer of Spray Falling Films over Horizontal Tubes with Counter Current Airflows in an Evaporative Condenser

Yee-Ting Lee [a, b], Chih-Yung Wen [c], Liang-Han Chien [a, b], Jiacheng He [d] and An-Shik Yang [a, b]*

[a] Department of Energy and Refrigerating Air-Conditioning Engineering, National Taipei University of Technology, Taipei 106, Taiwan
[b] Research Center of Energy Conservation for New Generation of Residential, Commercial, and Industrial Sectors, National Taipei University of Technology, Taipei 106, Taiwan
[c] Department of Mechanical Engineering, The Hong Kong Polytechnic University, Kowloon, Hong Kong
[d] School of Material and Energy, Guangdong University of Technology, Guangzhou 510006, China

Mailing Address:
Dr. An-Shik Yang (*Corresponding Author)
Distinguished Professor and Department Chairman
Department of Energy and Refrigerating Air-Conditioning Engineering
National Taipei University of Technology
1, Sec. 3, Chung-Hsiao E. Rd., Taipei 106, Taiwan
Tel: (886) 2-2771-2171 ext. 3523
Fax: (886)2-2731-4919
Email: asyang@ntut.edu.tw

Keywords: Spray falling film, Film evaporation, Counter current airflows, CFD simulation

Abstract

The spray film evaporative cooling equipment is useful to circumvent the scaling with expanded liquid coverage for attaining good thermal performance and energy efficiency. This paper examines the evaporative heat transfer phenomena of falling spray films over the horizontal circular tube array. In the experimental study, a high-speed camera with a LED fiber optic light source is implemented to capture the optical images for illuminating the distributions of spray films over the tube array under the counter current airflows. The average wall temperature, outlet temperature of spray nozzle and heat flux regulated by a programmable DC power supply are measured to determine the heat transfer coefficient. Moreover, the computational simulation is conducted using the CFD software ANSYS/ Fluent® in conjunction with a user defined function (UDF) to investigate the evaporative heat transfer of liquid spray films over the tubes. The calculated liquid film thicknesses and average heat transfer coefficients around the upper and lower tubes agree reasonably with the measured data to validate the numerical model. To explore the development of falling spray film dispersion and thermal performance over the tubes, the measurements and simulations are then extended to examine the characteristics of film thickness and heat transfer of splashed water sprays on the tube array at varying water flow rates of 3-7 l/min, heat fluxes of 10-50 kW/m^2, tube placement positions of 0-142.5 mm (i.e. w1-w6) and counter current airflow velocities of 0.8-2.0 m/s, respectively. In measurements, the average heat transfer coefficients of four positions for the tubes at an upward airflow velocity of 2 m/s can reach 5.0 kW/m^2 K for the water flow rate of 5 l/min and a heat flux of 30 kW/m^2K.

Keywords: Spray falling film, Film evaporation, Counter current airflows, CFD simulation

1. Introduction

With the rapid progress of data centers and information equipment for telecommunications and storage systems, it is estimated that electricity utilized by such facilities is around 1.4% of total world consumption [1]. As an environmental friendly, effective and economic cooling solution, the evaporative condenser has the advantages of compact structures allowing for easy maintenance in both water- and air-cooled utilizations [2]. Therefore, the application of evaporative condenser has significant engineering implications in handling harsh cooling load with low energy consumption [3]. Substantial endeavors by numerical and experimental analyses have been conducted to explore the thermofluid behaviors of evaporative condensers. Parker and Treybal [4] firstly demonstrated a detailed analysis of counter-flow evaporative liquid coolers based on four operational modes. They devised the empirical correlations of heat and mass transfer characteristics of an evaporative cooler having 19-mm diameter horizontal circular tubes. Their study then established a base for following theoretical and experimental works of heat and mass transfer in an evaporative cooler. Mizushina et al. [5], Dreyer and Erens [6], Niitsu et al. [7] and Hasan and Sirén [8] installed a variety of configurations and sizes of evaporative condensers for performance evaluations. These researchers

analyzed the effect of tube diameter on the thermal outcomes of the evaporative cooling devices to develop the empirical correlations for the heat and mass transfer. Furthermore, Ettouney et al. [9], Hosozet al. [10] and Hajidavalloo et al. [11] reported similar findings. They pointed towards that an evaporative condenser retains the features of an elevated thermal load, a higher COP and a greater seasonal energy efficiency ratio, as compared to an air-cooled condenser. Heyns and Kröger [12] experimentally investigated the thermodynamic performance of a counter-flow evaporative cooler. The obtained results showed the spray water mass flow rate as the most significant factor affecting the development of spray films, with the water film-air mass transfer coefficient correlated to the mass flow rates of the air and spray water. Finlay and Harris [13] formulated a simulation model to examine the features of the coil set in evaporative cooling for two types of the traditional closed loop evaporative cooler and an air-cooled-evaporated composite cooler. Islam et al. [14] conducted both experimental and numerical analyses to explore the film dispersion process in an evaporative condenser for an air-conditioning system. The experimental results reveal an increase in COP of the evaporately-cooled air-conditioning by around 28% compared with the conventional cooler unit.

For industry utilization of spray films, the water distribution method of spray type dominates the market. Moreover, in the practical use of evaporative condensers, it is easy to derive fouling and corrosion if the water flow can’t be effectively and evenly distributed in the process of sprinkling water. Al-Zubaydi et al. [15] inspected the effect of a novel water spray configuration on the ventilation energy recovery performance of indirect evaporative coolers (ICE). Three water spray modes were tested involving the external spray, internal spray and mixed spray. Here the external spray mode indicates the hollow cone nozzles arranged perpendicularly over the entrance of the wet channels, while the internal spray mode represents the flexible PVC tube with multiple spraying holes inserted inside the wet channels. The mixed spray mode combines the external spray and internal spray methods together to attain the indirect evaporative cooling outcomes, suggesting the best results of the mixed spray mode. The mixed mode improves the performance further by increasing wettability. Furthermore, the internal spraying in conjunction with increasing wettability can perform better than the external spray mode. The researchers from Baltimore Aircoil Co. [16] proposed a patent to attain the uniform water spray distribution for improving the sprinkler efficiency, and thereby reduce the possibility of scale generation on the coil. De Antonellis et al. [17] measured the thermal performance of an indirect evaporative system. The cooling outcomes are strongly influenced by the water flow rate but slightly affected by the nozzle number and size. With the same test conditions, more heat is transferred using the nozzles in a counter-flow arrangement than in a cross flow scenario. Experiments were performed by Chien et al. [18] to investigate the uniformity of water sprays and collection ratio of sprinkler in an evaporative condenser of a water chiller. Having three different combinations of nozzle opening length and width tested at the flow rates of 135-176.4 LPM, the measured results reveal the significant influences of cross-sectional area of nozzle opening and flow rate on the uniformity of water sprays. At elevated flow rates, the nozzle opening of 4-cm length and 1-cm width tends to produce

more even water sprays. Moreno et al. [19] assessed the cooling performance of three different nozzles, including a single hollow cone spray nozzle, a 2×2 jet array spray nozzle and a 4×4 jet array spray nozzle, with gassy-subcooled FC-72 as the working fluid. The obtained results infer that the variation of nozzle-to-heater spacing affects heat transfer rates more than critical heat flux (CHF).

From the above literature review, industry utilization of spray films has been demonstrated to be more effective for operations in evaporative cooling equipment because of evading the clogging problem and expanding the water spray coverage of liquid film distribution [20-23]. Substantial efforts have been made to explore the inter-tube flow patterns of drip, droplet and sheet modes, liquid film thickness distribution and evaporative heat transfer performance through typical liquid inlet feeders. As compared to the scenarios of falling films under spray impingements, it is relatively easier to conduct the experimental and numerical studies for probing the falling film characteristics. Most former studies on spray nozzles were focused on investigating the atomization mechanisms, spray cone angle of jet nozzle and droplet size distributions. Very little attention has been paid to examining the spray films over horizontal tubes by impinging liquid sprays. In our previous paper [22] probed the liquid film dispersion behaviors on the horizontal tubes under spray impingements. The close-up observations and measurements revealed the complex two-phase flow processes for the expansion of liquid fans, impingement of ejected sprays and progression of spray films. Besides, we also applied the computational fluid dynamics (CFD) simulation based on the volume of fluid (VOF) method to characterize the behaviors of interfacial movements. The studied results have also fully addressed the effects of inlet water flow rate and tube placement position on the intertube flow modes of spray films and film thickness distributions over horizontal tubes. As a continuing study, the purpose of this paper is to explore the flow transport and thermal behaviors of spray films over horizontal circular tubes. Experimentally, the liquid film thicknesses are measured via the image analysis of photographed high-speed optical pictures. The heat flux is varied using a programmable DC power supply to investigate heat transfer coefficients of upper/lower test tubes at different water flow rates and placement positions of tubes. The measurements are extended to assess the thermal outcomes of the evaporative condenser with counter current airflows. Moreover, the numerical analysis is performed applying the CFD software ANSYS/Fluent® in conjunction with a user defined function (UDF) to simulate the evaporative heat transfer of liquid spray films on horizontal tubes. To validate the numerical model, the predictions are compared against the measured liquid film thicknesses and average heat transfer coefficients around horizontal circular tubes. The formation process of spray film dispersion and heat transfer characteristics over the tubes are then explored to attain physical insight into the development of evaporative condensers.

2. Experimental measurements

2.1 Apparatus and procedure

Fig. 1 exhibits a schematic of the test facility. The apparatus primarily includes the spray

nozzles, a thermostatic bath, a heating part, measurement instruments, power and recovery units. The experiments are conducted using deionized water at a temperature of 25°C and 1 atm pressure. In the water flow loop, a constant liquid level is maintained at the bottom of a 50-cm tall acrylic water tank. We utilize a pump (TW-75500-00, Cole-Parmer) to drive the continual water flows. Two T-type thermocouples (Omega Engineering) and a pressure sensor (PT001, TBT) are exploited to measure the inlet temperatures and pressure at a nearby upstream location of spray nozzles. The liquid flow rates are controlled using two calibrated rotameters (TW-32005-14, Cole-Parmer), while the fluid temperature is controlled by a thermostatic bath (Alpha RA24, LAUDA). All connecting pipes are wrapped with thick thermal insulation materials to minimize heat loss. By the three-dimensional (3D) printing technique, the inner diameter and height of a fabricated spray nozzle are 12.4 mm and 40 mm. The width, height and opening angle of an outlet injection orifice are 11.98 mm, 3.12 mm and 13.5^{o}, respectively. The liquid flows into the spray nozzles with a wide discharge outlet to dispense the ejected liquid fan sheets for ensuing head-on impingements, and then sprays on the outside surfaces of the tube bank. Afterwards, the falling liquid splashes are collected in the water tank for recirculation. A LED fiber optic illuminator (SLG-165V, REVOX) operates as a light source to provide high light uniformity over the image plane. A high-speed camera (IL5-H, FASTEC Imaging) with a 17-mm F/0.95 lens (DO-1795 high-speed video lens, Navitar) grabs the visualized images of spray film flow patterns at a frame rate of 643 frame/s (fps) with a spatial resolution of 1920(H)×1080(V) pixels to realize a 5-μm pixel size. This research applies the manual measurement function from the image processing software IC Measure® (The Imaging Source) to characterize the thickness distributions of spray films quantitatively around each horizontal test tube [22, 24]. A more detailed description on experimental setup can be found in our previous work [22]. During the experiments, we control the constant water flow rates at 3, 5 and 7 l/min for each spray nozzle. The heat flux caused by the heating part is varied by a programmable DC power supply (62002P-100-25, Chroma) to achieve a range of 10-50 kW/m^2. Furthermore, for the counter airflow test, twelve fans (Sunon, HAC0251S4-0000-C99) are placed at the top of the test container constructed using acrylic plexiglass panels to introduce upward airflows across the test section, keeping the uniformly stable velocities of 0.8, 1.4, and 2.0 m/s with the root mean square deviation well within 4.8 % at ambient pressure. The period in measurements of temperature is at least 30 min with the interval recordings for every 1 s to reach the steady state in the test scenarios. Table 1 summarizes the instrument name, model number, measurement range, precision and manufacturer of each measuring device used in the experiment.

Table 1. Specifications of measuring instruments

Instrument	Model number	Range	Precision	Manufacturer
Pump	TW-75500-00	1.0–80 l/min	±5.0% RD	Cole-Parmer
Rotameter	TW-32005-14	1.2–12 l/min	±5.0% RD	Cole-Parmer

Pressure sensor	PT001	0–70 kPa	±0.20% FS	TBT
Temperature sensor	T-type thermocouple	-100 °C–400°C	±0.10 K/°C	Omega Engineering
Thermostatic bath	Alpha RA24	−25 °C–100 °C	±0.05 °C	Lauda
DC power supply	62002P-100-25,	0–100 V; 0–25 A	±0.20% FS	Chroma
Fan	HAC0251S4-0000-C99	0–24 V; 0–570 mA	±1% FS	Sunon
LED fiber optic illuminator	SLG-165V	100–240 V; 0–25 A	±15% FS	REVOX
High-speed camera	IL5-H	1920(H)×1080(V); 643 (fps)	5-μm pixel size	FASTEC Imaging

RD: Reading; FS: Full scale

2.2. Test section

The test container is made of clear acrylic plexiglass panels with the inner dimensions of 0.38×0.38×1.13 m as an enclosed environment. The spray nozzles having an inner diameter/height of 12.4/40 mm are positioned with a distance of 95 mm between nozzle exits, whereas the vertical interval from the exits of two nozzles to the test section is 100 mm (in Fig. 2(a)). The test section primarily consists of two 19 mm diameter × 100 mm long smooth round copper cylinders as the upper and lower test tubes in a tube bank (in Fig. 2(b)). We drill a hole with an interior diameter of 8 mm and a depth of 95 mm to dispose a heater rod in the center of the circular cylinder. To measure the surface temperature of each cylinder, four T-type thermocouples are inserted into the small holes of 0.7 mm×60 mm (diameter × length), surrounding the center hole. Those tubes are mounted horizontally on a vertical steel plate with the tube-to-tube spacing of 2.85 mm. As the preparation measures, we first use emery paper (#2000) to carefully polish each copper cylinder for eliminating an oxidized layer, and then cleanse the cylinders with copper oil. The cylinders are further rinsed in ethanol and deionized (DI) water, with their surfaces purged with nitrogen gas. The heat transfer performance can be appreciably affected by the tube placements. This study pinpoints the tube bank underneath the center amid two spray nozzles as the baseline setting of w1, and shifts from the center toward its left side split into 6 equally spaced points (i.e., w1, w2, w3, w4, w5 and w6) with a 9.5-mm interval (in Fig. 2(c)).

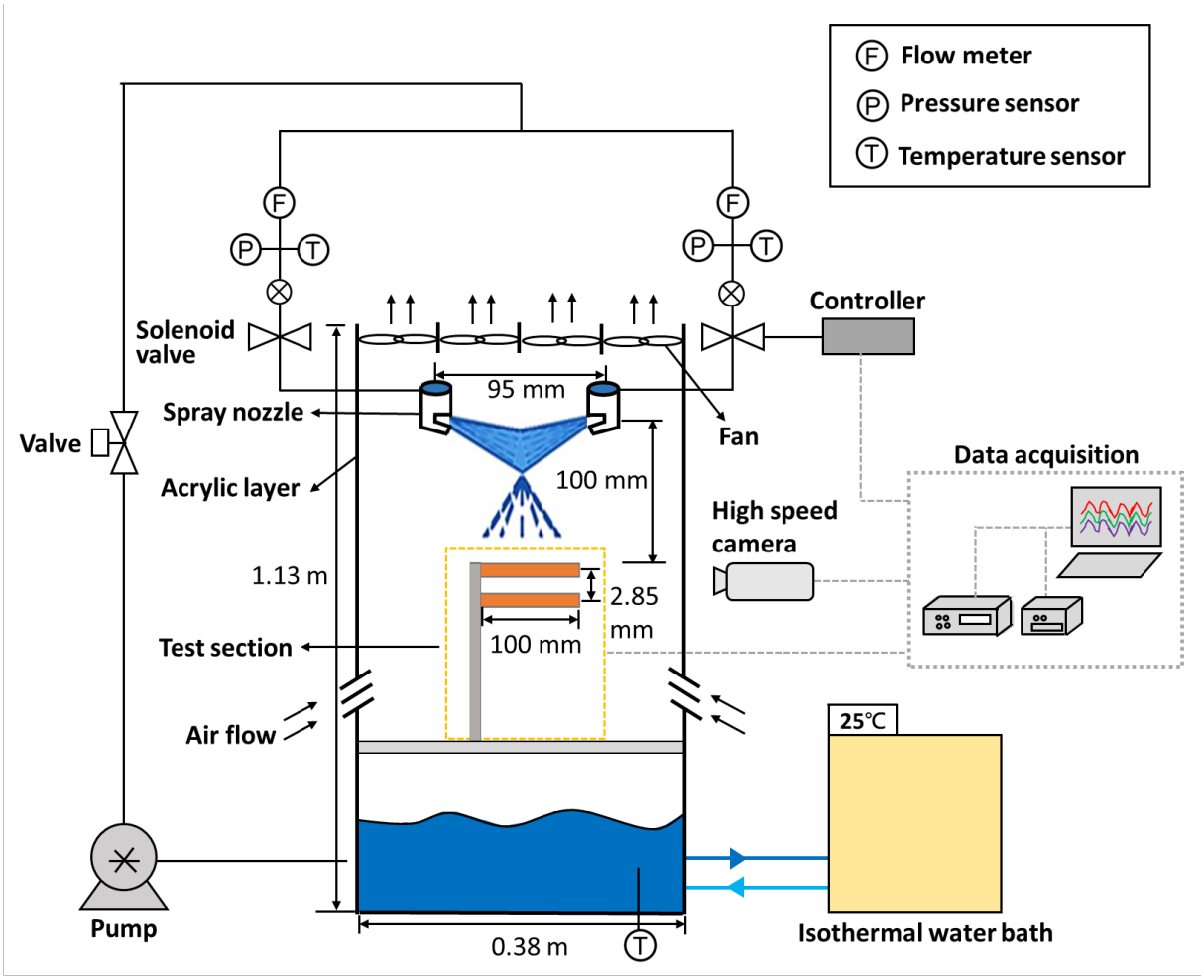

Fig. 1 Schematic diagram of experimental setup

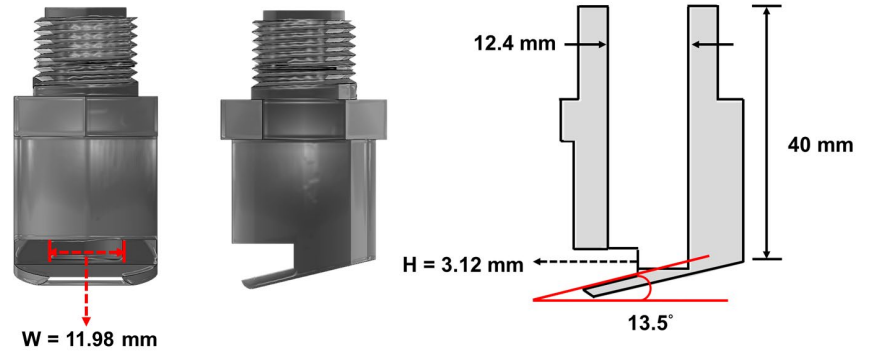

(a)

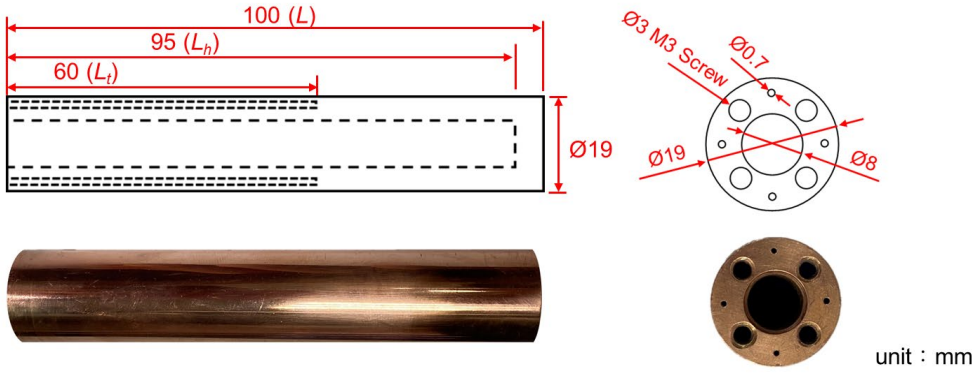

(b)

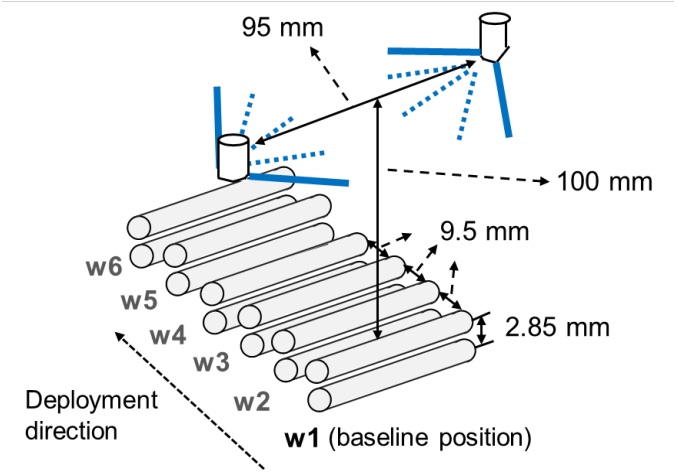

(c)

Fig. 2 Details of test section: (a) two spray nozzles in front, side and cross-sectional views, (b) design drawings and pictures of a machined test tube, and (c) positions of w1 to w6 for tube placement

2.3 Data processing and uncertainty

The thermal performance of a tube bank can be assessed by defining the average heat transfer coefficient h_{ave} as:

$$h_{ave} = \frac{q_{eff}}{T_{w,ave} - T_o}, \tag{1}$$

where q_{eff} is the effective heat flux in terms of the footprint heating area in Eq. (2). $T_{w,\,ave}$ represents the average wall temperature, and T_o is the average outlet temperature of spray nozzles. The heat flux can be then expressed as,

$$q_{eff} = \frac{Q}{\pi d L}. \tag{2}$$

The amount of the total heat generated in the heating rod (Q) is evaluated using the measurements of the supplied voltage and the current of the element. The heated surface area (the heated outer

surface) of each test tube, where d is the outer diameter of the test tube and L is the effective heated length of the tube.

The experimental uncertainties of the heat flux and pressure drop are estimated using the method suggested by Moze [25] and Hong [26]. The uncertainties in the programmable DC power supply and the dimension of the test tube are ±0.20% full scale (600 W) and ±0.01 mm. The smallest heat load is 119 W with the diameter of 19 mm for the test tube in the present study, and the maximum uncertainty of the heat flux is thus given as follows:

$$\frac{\partial q_{eff}}{q_{eff}} = \pm\sqrt{\left(\frac{\partial Q}{Q}\right)^2 + \left(\frac{\partial A}{A}\right)^2} = \pm\sqrt{\left(\frac{0.2\% \times 600}{119}\right)^2 + \left(\frac{0.01}{19.0}\right)^2} = \pm 1.0\% . \tag{3}$$

The uncertainties of the rotameter and thermocouple are ±5.0% reading (= $\partial V/V$) and ±0.1 K, respectively. The lowest measured temperature difference between wall temperature and outlet temperature of spray nozzles is 1.66 K in this work. Therefore, the maximum uncertainty of heat transfer coefficient is given by:

$$\frac{\partial h}{h} = \pm\sqrt{2\left(\frac{\partial V}{V}\right)^2 + \left(\frac{\partial q_{eff}}{q_{eff}}\right)^2 + \frac{(\partial T_{w,ave})^2 + (\partial T_o)^2}{(T_{w,ave} - T_o)^2}}$$

$$= \pm\sqrt{2(5.0\%)^2 + (1.0\%)^2 + \frac{(0.1)^2 + (0.1)^2}{(1.66)^2}} = \pm 11.1\% . \tag{4}$$

As a result, the uncertainties of heat flux and heat transfer coefficient estimated through the measurement results are ±1.0% and ±11.1%, respectively.

3. Numerical approach

3.1 Governing equations and numerical method

In this study, ANSYS/Fluent® 18.0 is applied to solve the governing equations with boundary conditions. The numerical analysis is based upon the time-dependent, 3D conservation equations of mass, momentum, energy and species concentration of water vapor throughout the development of spray falling films.

$$\nabla \cdot \vec{V} = \left(\frac{1}{\rho_v} - \frac{1}{\rho_l}\right)\dot{m}\left|\nabla \alpha\right|, \tag{5}$$

$$\frac{\partial \alpha}{\partial t} + \nabla \cdot \left(\vec{V}\alpha\right) = \frac{1}{\rho_v}\dot{m}\left|\nabla \alpha\right|, \tag{6}$$

$$\frac{\partial}{\partial t}\left(\rho\vec{V}\right) + \rho\vec{V} \cdot \nabla\vec{V} = -\nabla p + \nabla \cdot (\mu_{eff}\nabla\vec{V}) + \rho\vec{g} + \vec{F}_\sigma , \tag{7}$$

$$\frac{\partial(\rho E)}{\partial t}+\nabla\cdot\left(\rho E\vec{V}\right)=\nabla\cdot\left(\lambda_{eff}\nabla T\right)+\dot{m}\left|\nabla\alpha\right|h_{lv}, \tag{8}$$

$$\frac{\partial(\rho_v Y)}{\partial t}+\nabla\left(\rho_v\vec{V}Y\right)=\nabla\cdot(\rho_v D_{eff}\nabla Y)+\dot{m}\left|\nabla\alpha\right|, \tag{9}$$

here the signs $\vec{V}$, α, ρ_l, ρ_v, p, ρ, T, Y, μ_{eff}, λ_{eff}, D_{eff} and t denote the velocity vector, volume fraction of liquid water, density of liquid/vapor water, pressure, density ($\rho = \alpha\rho_l+(1-\alpha)\rho_g$), temperature, mass fraction of water vapor in the mixture gas, effective viscosity ($\mu_{eff} = \alpha\mu_{eff,l}+(1-\alpha)\mu_{eff,g}$), effective thermal conductivity ($\lambda_{eff} = \alpha\lambda_{eff,l}+(1-\alpha)\lambda_{eff,g}$), effective diffusion coefficient ($D_{eff} = \alpha D_{eff,l}+(1-\alpha)D_{eff,g}$) of the mixture fluid and time, respectively. The momentum source terms involve the forces of gravity ($\rho\vec{g}$) and surface tension ($\vec{F}_\sigma$) related to the interfacial phenomena (in Eq. (7)). The continuous surface force (CSF) formulation is implemented to model the surface tension effect as a localized volumetric force over a numerical cell as follows [27-29].

$$\vec{F}_\sigma = \sigma\kappa\vec{n}\left|\nabla\alpha\right|. \tag{10}$$

The symbol σ signifies the surface tension between the liquid and vapor phases, while its value is 0.0735 N/m for water in this case. Moreover, κ is the average interfacial curvature with the surface tension force acing along the normal axis ($\vec{n}$) of the liquid surface. The term $\left|\nabla\alpha\right|$ is present only in the interfacial variation region with the variable α varying from 0 to 1. This study uses the volume-of-fluid (VOF) method to track the movements of interface by the liquid volume fraction (α) distribution, with the contour of α= 0.5 to pinpoint the interfacial position in the transient water-moist air flow process for the visualization purpose. The above VOF calculations in conjunction with reconstructing free surfaces via the piecewise linear interface construction (PLIC) technique are conducted to capture interfacial movements during the dispersal evolution of spray films [30, 31]. In Eq. (8), energy is expressed as $E = (\alpha\rho_l E_l+(1-\alpha)\rho_v E_v)/\rho$, and Eq. (9) is employed to calculate the vapor pressure at the interface. The energy source term ($\dot{m}\left|\nabla\alpha\right|h_{lv}$, h_{lv} is the latent heat of vaporization) describes the heat transfer associated with the evaporative mass flux ($\dot{m}$) at the liquid film surface to the environment. For the proportional relationship of the evaporating flux relating to the difference between the saturation pressure at the liquid water temperature and the water vapor pressure in the air enclosing the tube, the Hertz–Knudsen equation is utilized to calculate the mass flux across the water-air interface in the vaporization course [32]. A user defined function (UDF) to calculate $\dot{m}$ is developed via Eq. (11) and incorporated into the governing equations as a source term.

$$\dot{m}=\frac{2\sigma_e}{2-\sigma_e}\left(\frac{M}{2\pi RT_{lv}}\right)^{0.5}\left(p_{v\_equ}(T_{lv})-p_v\right). \tag{11}$$

Here σ_e, R, M, p_v and $p_{v\_equ}(T_{lv})$ stand for the accommodation coefficient, universal gas constant (8.314 J/mol-K), molecular weight of water (18.015 g/mol), vapor pressure and equilibrium vapor pressure referring to the interfacial temperature T_{lv}. From the experimental and theoretical studies for a widespread diversity of substances, the value of σ_e is affected by the fluid, geometry, boundary conditions and even mesh size, whereas a large σ_e value tends to cause the numerical difficulties of convergence [33, 34]. In this study, the accommodation coefficient σ_e is resolved by a trial-and-error procedure and specified as 0.001. Moreover, the symbol $p_{v\_equ}(T_{lv})$ denotes the equilibrium vapor pressure corresponding to the interfacial temperature T_{lv}. Eq. (11) can be derived from the kinetic theory to compute the evaporating vapor flux correlated with the interface temperature and vapor pressure. The equilibrium vapor pressure $p_{v\_equ}(T_{lv})$ can be expressed as follows.

$$p_{v\_equ}\left(T_{lv}\right) = P_{sat\_ref}\left(T_{ref}\right)\exp\left[\frac{Mh_{lv}}{R}\left(\frac{1}{T_{ref}}-\frac{1}{T_{lv}}\right)\right], \tag{12}$$

where T_{ref} is the reference temperature of 298.15 K. As the corresponding saturation vapor pressure, $p_{sat\_ref}(T_{ref})$ is equal to 3169.9 Pa

This study considers the spray falling film flows as turbulent flows owing to the film Reynolds number ($Re= 4\Gamma/\mu_l$) up to 5375 [22]. Since the turbulence effect is of great importance in the heat transfer outcomes of spray films [31], several published papers [35-37] have successfully applied the SST k-ω turbulence mode to the studies of film dispersion of liquid sprays on a horizontal tube. As one of the major drawbacks of k-ε modeling, turbulence models based on the ε-equation can generally over-predict the turbulent length scale in the flows with adverse pressure gradients, leading to elevated wall shear stresses and high heat transfer rates [38]. Alternatively, the shear stress transport (SST) model benefits from the advantages of the k-ω and standard k-ε models by modifying the eddy-viscosity term for improving simulation capabilities of the model in adverse pressure boundary layers [39]. Additionally, our previous study demonstrated the accurate predictions of the SST k-ω turbulent model in liquid film spreading computations [37]. As a result, this study adopts the SST k-ω turbulent model for turbulence closure in simulations. The governing equations are shown as follows:

$$\frac{\partial \rho k}{\partial t}+\nabla\cdot\left(\rho k\vec{V}\right)=\nabla\cdot\left(\left(\mu+\frac{\mu_t}{\sigma_k}\right)\nabla k\right)+\mu_t S^2-\beta^*\rho\omega k \tag{13}$$

$$\frac{\partial \rho \omega}{\partial t}+\nabla\cdot\left(\rho\omega\vec{V}\right)=\nabla\cdot\left(\left(\mu+\frac{\mu_t}{\sigma_\omega}\right)\nabla\omega\right)+\frac{aa^*}{\nu_t}\mu_t S^2-\beta\rho\omega^2+2(1-F_1)\frac{\rho}{\omega\sigma_{\omega 2}}\nabla k\nabla\omega \tag{14}$$

In Eqs. (13) and (14), the sign μ_t denotes turbulent viscosity as $\mu_t = (\rho k/\omega)[1/\max(1/a^*, SF_2/a_1\omega)]$; σ_k $\left(=\left(F_1/\sigma_{k1}+\left(1-F_1\right)/\sigma_{k2}\right)^{-1}\right)$ and σ_ω $\left(=\left(F_1/\sigma_{\omega 1}+\left(1-F_1\right)/\sigma_{\omega 2}\right)^{-1}\right)$ are the turbulent Prandtl numbers. Here $\mathrm{Re_t}= \rho k/\mu\omega$, $S=\sqrt{2S_{ij}S_{ij}}$ and S_{ij} is the shear strain rate. And a $\left(a=\frac{a_\infty}{a^*}\left(\frac{a_0+\mathrm{Re}_t/R_\omega}{1+\mathrm{Re}_t/R_\omega}\right)\right)$ is a constant in

Eq. (14). The empirical constants $\sigma_{\omega 1}, \sigma_{k1}, \sigma_{\omega 2}$ and σ_{k2} in turbulent transport equations are 2.0, 1.176, 1.168 and 1.0, respectively. The detailed empirical closure functions of β, β^*, F_1, F_2, R_ω, a_∞, a_0, a^* and a_1 can be found in [40]. The pressure-implicit with splitting of operators (PISO) algorithm is implemented for the coupling of pressure and velocity [41]. In simulations, we use the second-order accurate upwind scheme to deal with the convective and diffusion terms. A first-order implicit scheme is employed for the unsteady term, while the volume fraction distribution is solved with an explicit time marching technique. This study applies the time-averaged practice ($\delta = \int_0^{t_{\text{int}}} \delta(t)dt / t_{\text{int}}$) to determine the liquid film thicknesses. The term $\delta(t)$ is the instantaneous value with the targeted interval (t_{int}) properly arranged to be ~1.5 times of the flow time (defined as the time needed for the dispensing liquid to flow through two test tubes) for achieving the adequate recurrences of the δ variation [22, 42]. We also employ the same process to calculate the heat transfer coefficient.

3.2 Geometric model and boundary conditions

Fig. 3 illustrates the computational domain and numerical grids with the magnified views around the tube surfaces for CFD simulations of impinged spray film development. The size of the model is 120 mm in length, 120 mm in width and 160 mm in height, respectively. Having the exits of spray nozzles specified as the liquid inlets, the vertical spacing between the nozzle exit and top rim of the upper tube is 100 mm in the z-direction. This study applies ANSYS Workbench® 18.2 to carry out the meshing arrangement, with structured hexahedral cells over the computational domain to comprehend the dispersion development of spray films. The mesh system primarily includes the regions of spray nozzles, liquid film dispersion area after spray impingement and horizontal round tubes. The average cell size within spray nozzles is around 0.55 mm with a grid expansion ratio of 1.1. Moreover, the mesh in the center area for the development of liquid impingement and spray films is refined having the average cell size of 0.75 mm. Besides, finer grids are disposed in the proximate surroundings of the tube walls (with the minimum cell size of around 0.012 mm) to predict the heat transfer results accurately in the dispersal progression of spray films. This study achieves the y^+ values of 0.63 and 0.67 for the first cells near the wall surfaces of upper and lower tubes. In particular, finer grids are arranged using the fully structured hexahedral elements in the near-wall regions around the circular tubes to ensure the orthogonality, smoothness and suitable aspect ratios for evading numerical divergence. The values of the minimum orthogonal quality, highest aspect ratio and peak cell skewness were 0.73, 5.20 and 0.69, respectively, suggesting the realization of a reasonably high quality mesh.

For the boundary conditions, two feeder openings of spray nozzles are set as the liquid inlets at the fixed velocities in consistent with the experimental settings of water flows. The tube surface temperatures are specified according to the measurements. The corresponding surface temperatures of upper/lower tubes are 302.5/303.3 K, 305.5/307.4 K and 306.8/309.7 K for the water flow rates of 3, 5 and 7 l/min at a heat flux of 30 kW/m^2. The still air is existent in the form of a full gas phase

for the other regions as the initial condition. The inlet water and initial air temperatures are prescribed as the atmosphere temperature of 25 °C. The pressure outlet boundary condition is specified as the ambient pressure of 1 atm given in the bottom plane. All the other boundary faces are arranged to be symmetric in calculations. The default contact angle is 0° to model a fully wetted wall condition [43, 44]. Table 2 shows the thermophysical properties of working fluids.

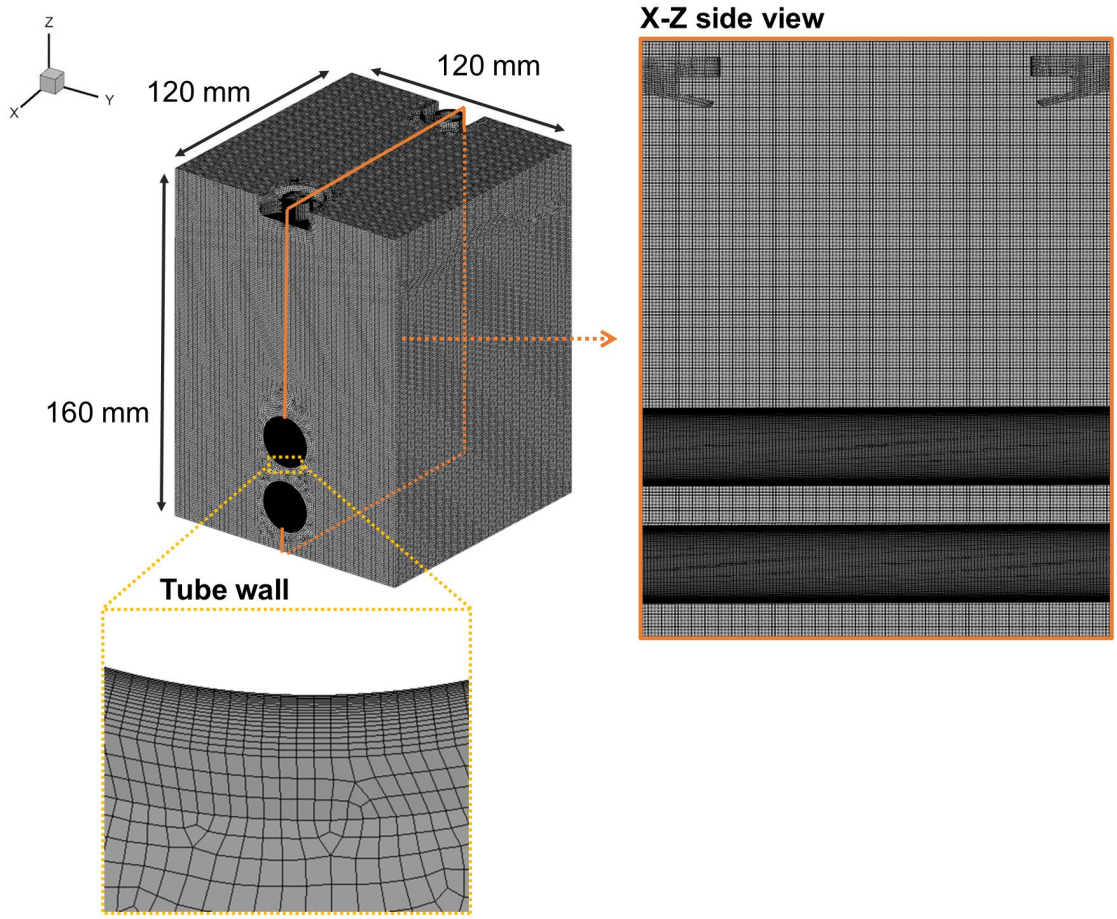

Fig. 3 Computational domain and numerical grids with magnified views around tube surfaces for CFD simulations of impinged spray film development

Table 2 Thermophysical properties of fluids

Fluid	Water-liquid	Water-vapor	Air
Molecular weight (kg/kmol)	18	18	29
Density (kg/m^3)	997.00	0.023	1.225
Specific heat (J/(kg·K))	4182	1912	1006
Thermal conductivity (W/m·K)	0.606	0.018	0.0242

Latent heat (kJ/kg)	2441.67	-	-
Diffusion coefficient	-	2.88×10^{-5}	-
Surface tension coefficient (N/m)	0.072	-	-
Viscosity (kg/(m·s)	89.0×10^{-5}	0.97×10^{-5}	1.78×10^{-5}

3.3 Mesh independence and model Validation

The grid-sensitivity study is performed to identify the optimum number of mesh elements for saving computational time without compromising accuracy. The simulations consider the fixed tube surface temperatures of 305.5 and 307.4 K for upper and lower tubes at a water flow rate of 5 l/min. Fig. 4 illustrates a comparison of the predicted liquid film thickness profiles with respect to the circumferential angle in the center plane (i.e., w1 position) for upper and lower tubes at three different (a) grids and (b) time steps. This study has completed the independency study of grid sensitivity with the total numbers of 4,613,702, 5,670,211 and 6,653,841 cells at the CFL value of 0.1 (with the corresponding time steps of 4.5×10^{-6} s, 4.1×10^{-6} s and 3.4×10^{-6} s). Utilizing the grids with the total numbers of 4,613,702, 5,670,211 and 6,653,841 cells, the peak differences of film thicknesses are up to 14.5%/13.1% for the upper/lower tubes between 4,613,702 and 6,653,841 cells, while the associated greatest discrepancies of predictions decrease to 5.3%/5.1% for 5,670,211 and 6,653,841 cells. Therefore, the mesh of 5,670,211 cells is selected to achieve more cost-effective solutions for the following thermal studies of spray films. To ensure the time accurate solutions, we also carry out the time step independency study at the Courant number (CFL) of 0.2, 0.1 and 0.05 (with the corresponding time steps ranging from around 1.2×10^{-5} to 9.6×10^{-7} s). The maximum variations of liquid film thicknesses are 6.1%/5.7% and below 1.4%/1.5% for the upper/lower tubes at CFL= 0.2 and 0.05 as well as 0.1 and 0.05. It suggests a negligible effect of a finer time step on the unsteady calculation results. Thus, the study arranges the mesh setup of 5,670,211 cells and CFL of 0.1 (with the associated time step of around 4.1×10^{-6} s) to achieve required accuracy in simulations.

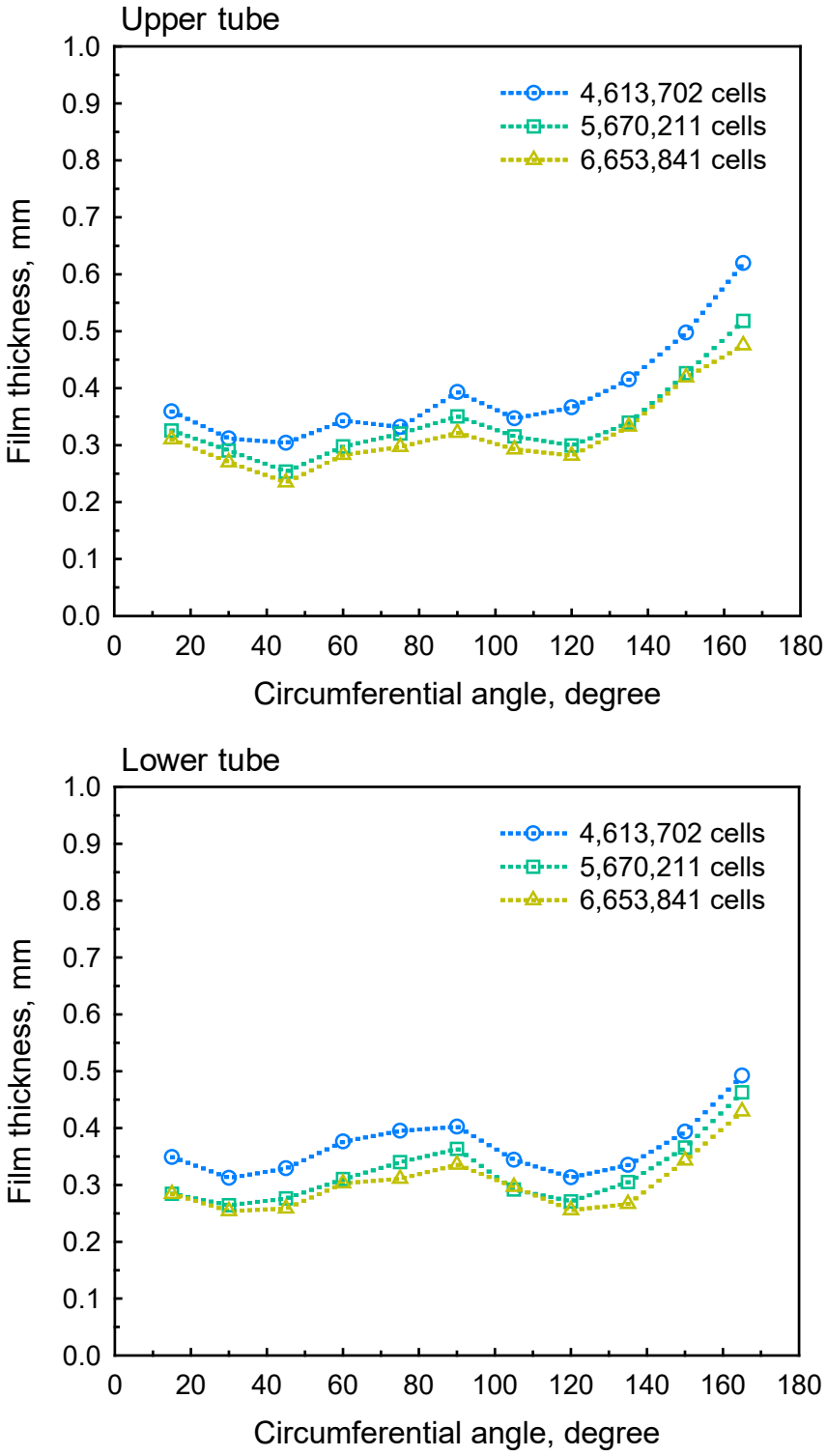
Upper tube
Film thickness, mm
Circumferential angle, degree
4,613,702 cells
5,670,211 cells
6,653,841 cells
Lower tube
Film thickness, mm
Circumferential angle, degree
4,613,702 cells
5,670,211 cells
6,653,841 cells

(a)

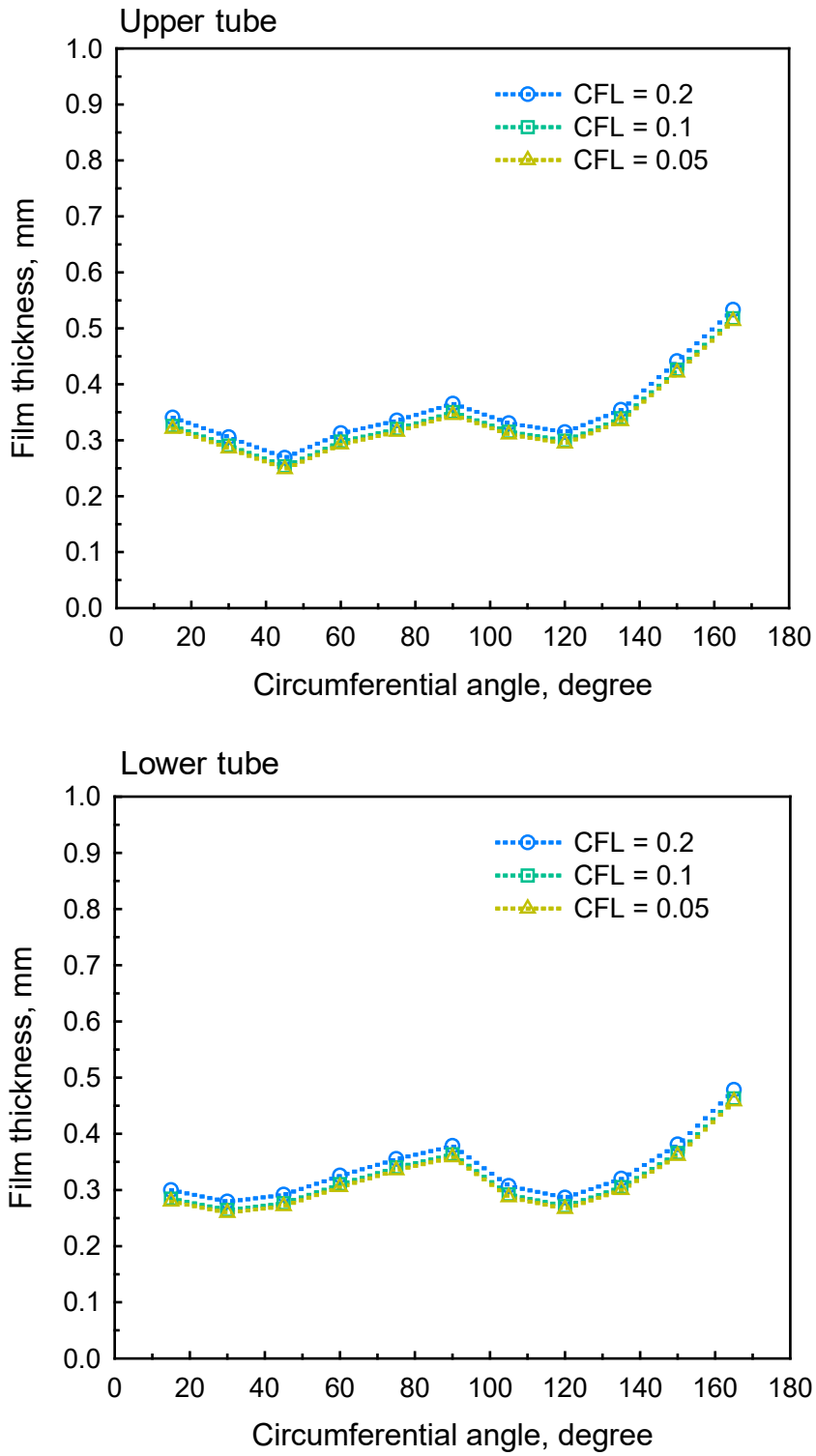

(b)

Fig. 4 Comparison of predicted liquid film thickness profiles with respect to circumferential angle at three different (a) grids and (b) time steps

To validate the present computational model, Fig. 5 exhibits a comparison of the predictions with measured (a) average liquid film thicknesses and (b) average heat transfer coefficients over

the outer surfaces of upper and lower tubes at the position of w1. For a test condition with the water flow rate of 5 l/min and fixed tube fixed heat flux of 30 kW/m^2, each data point denotes the mean value of 5 measured records of film thickness with the error bars specified by $\pm 3\sigma_{sd}$ (σ_{sd} is the standard deviation). Overall, the CFD results show similar tendencies with the measurements for both upper and lower tubes (in Fig. 5 (a)). The calculations underpredict the film thicknesses with relatively high errors, as compared to the measured data. Essentially, the mean deviations between the calculated film thicknesses and measurements on the upper and lower tubes are approximately 10.4% and 12.3%, respectively. In exploring the thermal outcome of spray films in Fig. 5 (b), the predictions of average heat transfer coefficient (ranging from 2.2 kW/m^{2}K to 5.0 kW/m^{2}K) are in fair agreement with the measurements. The associated mean differences are 16.3% to 15.7% for the upper and lower tubes, respectively.

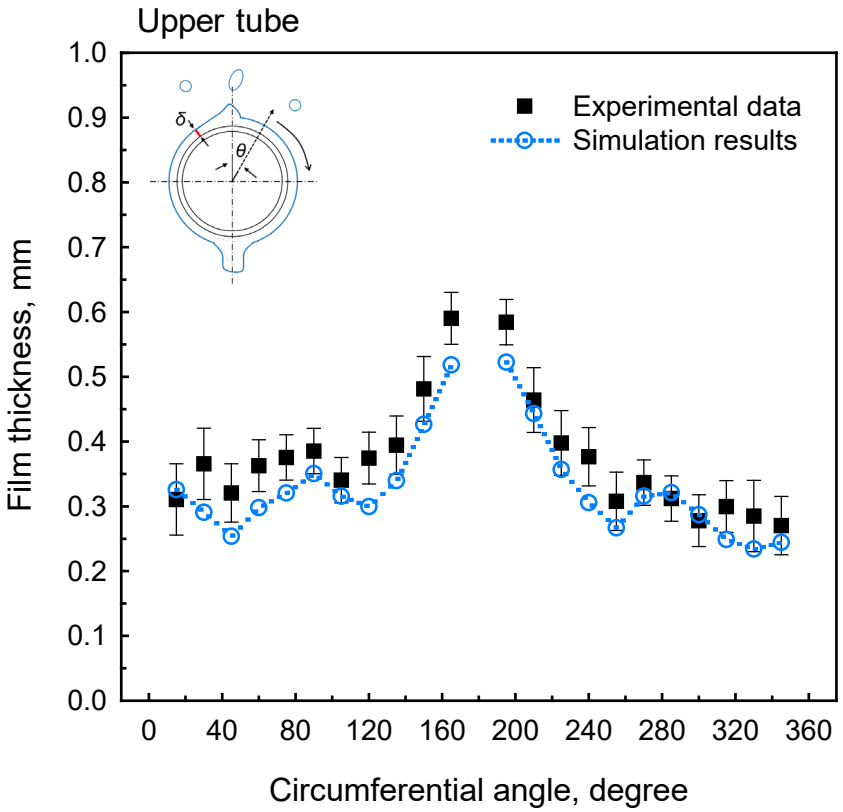

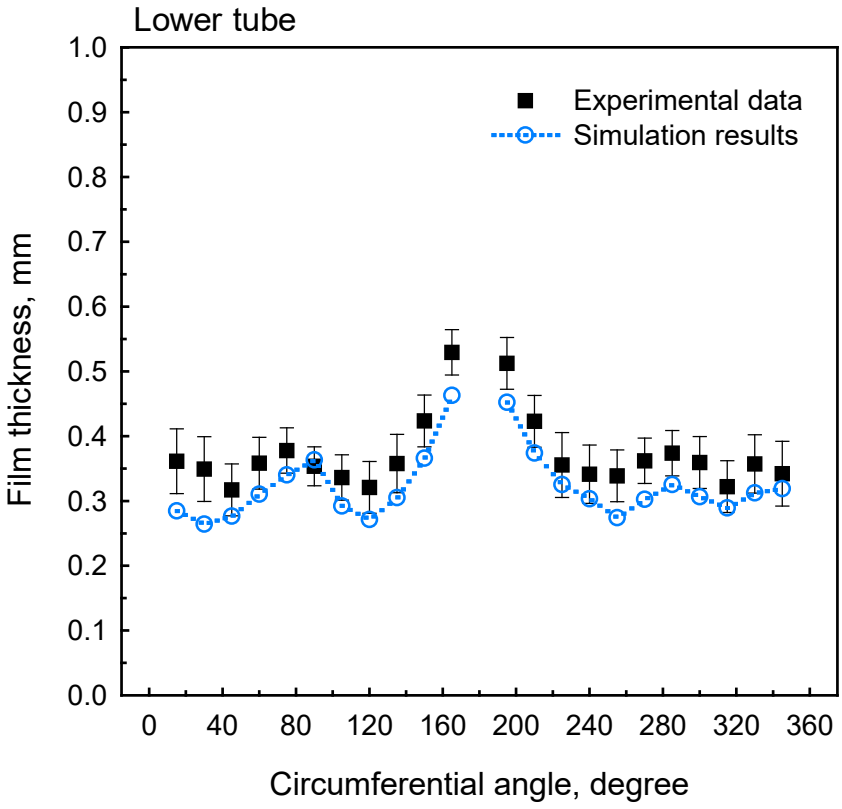
Lower tube
Experimental data
Simulation results
Film thickness, mm
1.0
0.9
0.8
0.7
0.6
0.5
0.4
0.3
0.2
0.1
0.0
0
40
80
120
160
200
240
280
320
360
Circumferential angle, degree

(a)

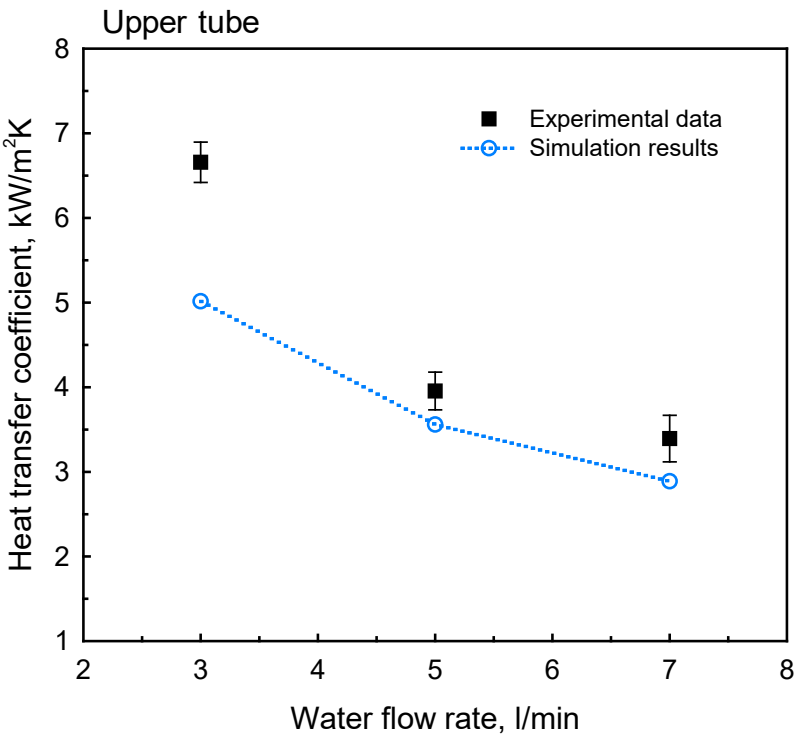
Upper tube
Experimental data
Simulation results
Heat transfer coefficient, kW/m2K
8
7
6
5
4
3
2
1
2
3
4
5
6
7
8
Water flow rate, l/min

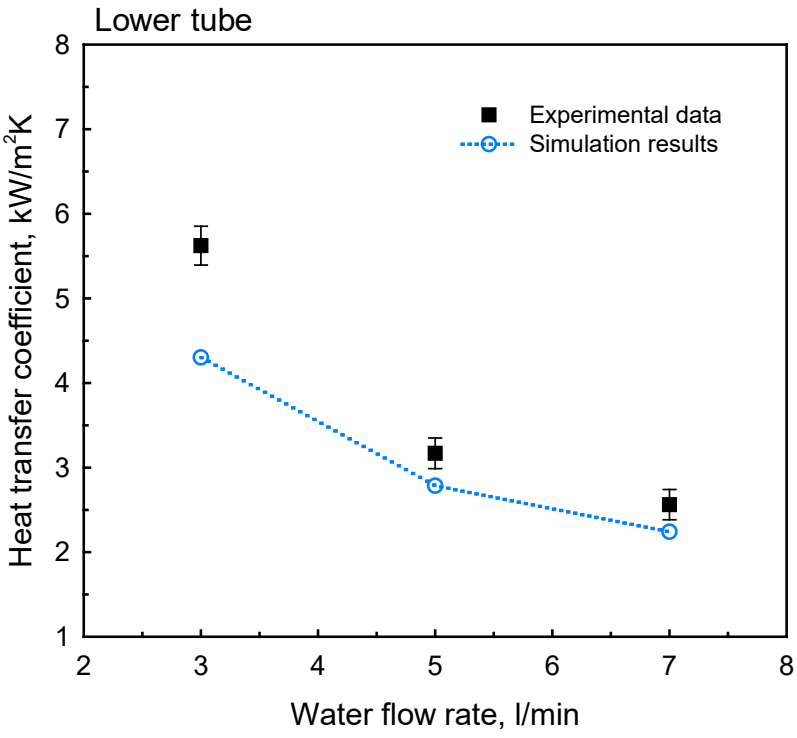

(b)

Fig. 5 Comparison of CFD predictions with measured (a) average liquid film thicknesses and (b) average heat transfer coefficients over the outer surfaces of upper and lower tubes at the position of w1 for a water flow rate of 5 l/min

4. Results and discussion

4.1 Effect of water flow rate

The experiments under the flow conditions of 3, 5 and 7 l/min are conducted via varying the heat fluxes to explore the thermal performance of spray films on the tube arrays. Fig. 6 shows the measured average heat transfer coefficients over the outer surfaces of upper and lower tubes at the position of w1 and a water flow rate of (a) 3, (b) 5 and (c) 7 l/min for varied heat fluxes. It is noted that the heat transfer coefficient is essentially enhanced with the increasing heat flux, and then reaches a plateau for three water flow rates. Moreover, in all cases, the upper tube can provide superior cooling performance than the lower one. For the scenario of 3 l/min, large volume water sprays falling on the center region (the w1 site) can produce better thermal outcomes having the values up to 6.6 and 5.6 kW/m^{2}K for both the upper and lower tubes, respectively. From our earlier research [22], we have learned that impinged jets at high water flow rates of 5 and 7 l/min tend to generate the higher horizontal fluid momentums, and thereby achieve more expanded areas of liquid sprays. The resultant lower amounts of water sprays are dispensed to the tubes placed at the w1 locality, showing the decline of heat transfer coefficients from 5.1-6.7 kW/m^{2}K at 3 l/min to 2.8-4.0 kW/m^{2}K and 2.4-3.4 kW/m^{2}K at 5 and 7 l/min.

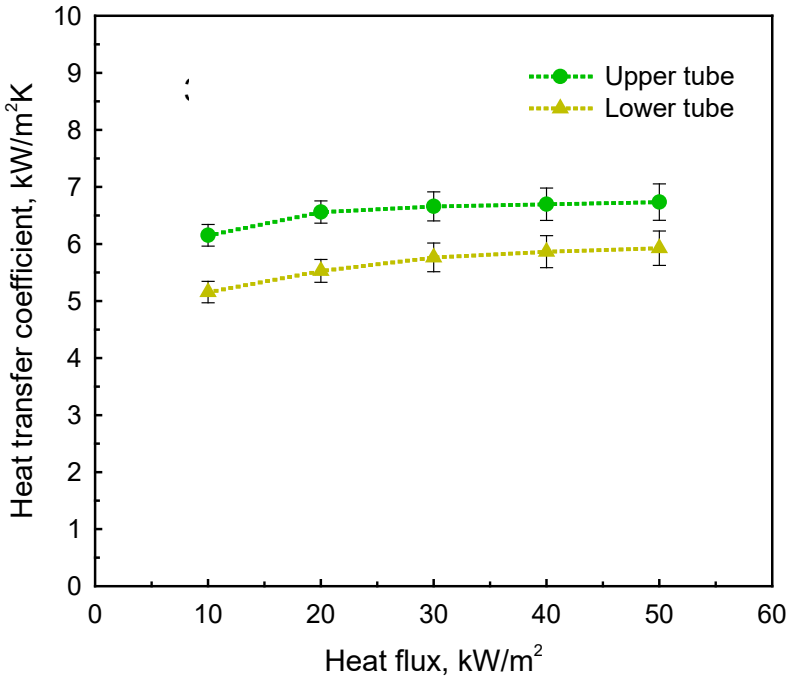
Upper tube
Lower tube
Heat transfer coefficient, kW/m²K
Heat flux, kW/m²
0
1
2
3
4
5
6
7
8
9
10
0
10
20
30
40
50
60

(a)

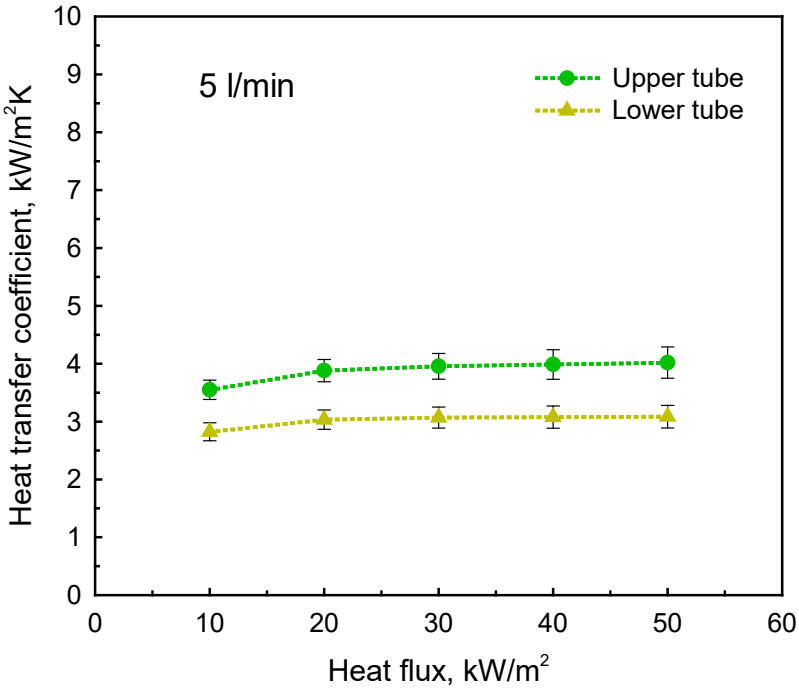
5 l/min
Upper tube
Lower tube
Heat transfer coefficient, kW/m²K
Heat flux, kW/m²
0
1
2
3
4
5
6
7
8
9
10
0
10
20
30
40
50
60

(b)

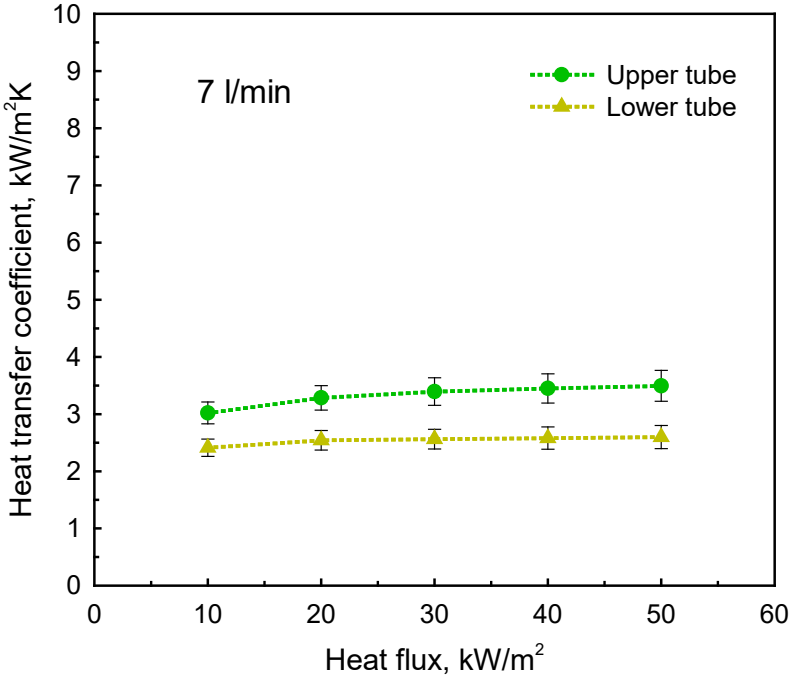

(c)

Fig. 6 Measured average heat transfer coefficients over outer surfaces of upper and lower tubes at the position of w1 and water flow rates of (a) 3, (b) 5 and (c) 7 l/min for varied heat fluxes

Because the detailed thermal and flow outcomes of spray films around the tubes are difficult to acquire experimentally, CFD simulations are useful to better understand the spreading behavior of liquid films and associated heat transfer characteristics over the circular tube array during the spray impingement process. Fig. 7 presents the predicted distributions of (a) heat transfer coefficient and (b) interfacial velocity magnitude over upper and lower tubes at the w1 position for the water flow rates of 3, 5 and 7 l/min. The liquid splashes falling after the jet collisions are relatively concentrated on the middle area at a low water flow rate of 3 l/min (in Fig. 7(a)). It should be noted that the CFD predictions of spray films marked in the red color indicate several spattered areas with high heat transfer coefficients (up to 20.8 kW/m^2K), appearing over the outer surfaces of upper and lower tubes in the core region. In contrast, the previous investigations of falling films [37, 42, 45] have pinpointed the highest thermal performance occurred only on the top area of the tube owing to the impingement heat transfer of liquid dripping. The cooling results then deteriorate with liquid films spreading toward both ends of two horizontal tubes. At the medium and high water flow rates of 5 and 7 l/min, the impingement of accelerated liquid jets tends to develop an expanded coverage of falling water sprays, showing less shed liquid fragments splattering over the upper tube surface in the mid locality. We visualize that those scattered areas of high heat transfer coefficients of 15-18 kW/m^2K (marked in the green-yellow colors) at a water flow rate of 3 l/min are relatively larger than those at a flow rate of 5 l/min in Fig.7(a), achieving a higher average heat transfer coefficient

of the test tubes.

In effect, the local heat transfer coefficient can be closely related to interfacial velocity [46, 47]. The forced thermal convection is essentially proportional to the velocity gradient of the liquid film; hence, the strong velocity gradient tends to produce high local heat transfer coefficient [44]. Having considerable amounts of water chunks falling on the tubes with incited saddle-shaped waves over liquid films at 3 l/min, the impacted liquid sprays tend to develop water films spreading along both the axial and circumferential directions over the tube surfaces. In Fig. 7(b), we view those irregular splashed areas with elevated interfacial velocities up to 1.5 m/s over the outer tube surfaces (upper center), producing superior thermal performance in the middle of tubes. Conversely, low interface velocities (≤0.3 m/s, marked by dark blue color) emerge on both sides of the upper tube. Afterward, the falling water films drip onto the lower tube at an interfacial speed of 0.6 m/s to enfold the entire tube. At 5 and 7 l/min, the expanded coverage of the falling water sprays results in liquid chunks (at a velocity up to 1.5 m/s) splashed onto the tubes, causing interfacial velocities of around 0.6-1.0 m/s.

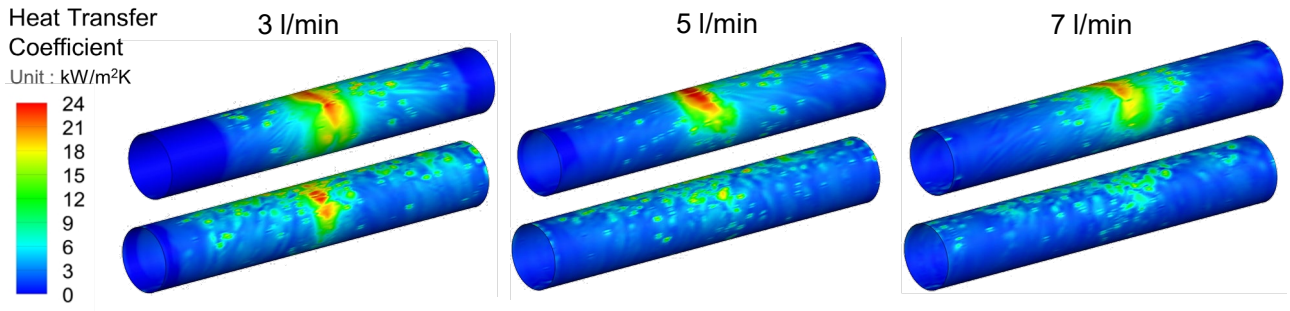

(a)

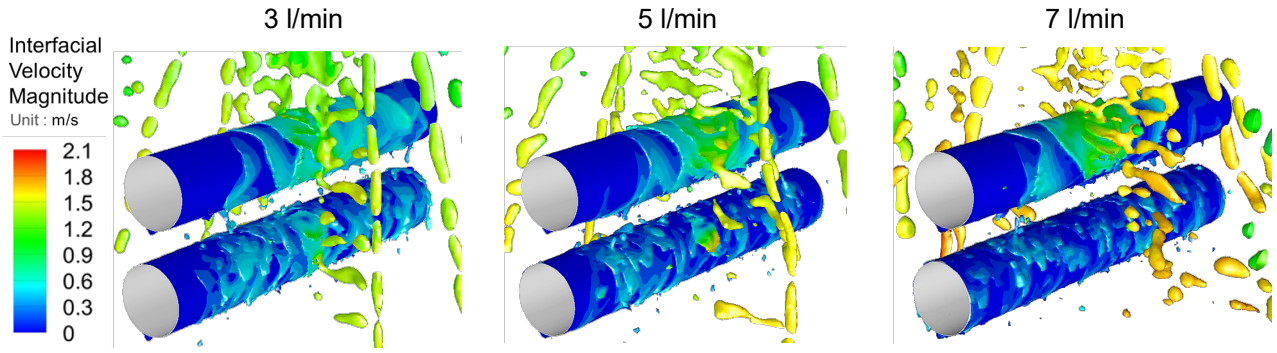

(b)

Fig. 7 Predicted distributions of (a) heat transfer coefficient and (b) interfacial velocity magnitude over upper and lower tubes at w1 position for water flow rates of 3, 5 and 7 l/min

Fig. 8 illustrates the predicted circumferential profiles of (a) heat transfer coefficient and (b)

interfacial velocity magnitude in the center plane of tubes at the w1 place for the water flow rates of 3, 5 and 7 l/min. This study selects the circumferential angle ranges of 15°-165° and 195°-345°to avoid the influences of fluctuating water sprays on the film thickness and thermal performance at the top and bottom regions of tubes. In essence, low water flow rates develop bulky liquid sprays plunging on the w1 station to realize the enhanced heat transfer results owing to elevated interfacial velocities around the tubes, as compared to those of high water flow rates. For instance, relatively high thermal outcomes are observed at 3 l/min over both tube surfaces in the center region. Unlike the scenario of falling spray films to produce the maximum heat transfer right at the impact point of liquid drops on the climax of the tube, the local heat transfer coefficients sustain above 20 kW/m^2K resulting from frequent impingements of water sprays in the extent of 15°-75°, and then persistently decline along the circumferential angles of the tubes. A nearly symmetric profile of heat transfer coefficient is also perceived from the opposite side (θ=195°-345°) of upper and lower tubes. High cooling performance can also be achieved at some angles due to the impingement of liquid blocks on the tubes from different directions. Alternatively, a high water flow rate of 7 l/min tends to form small-sized drops splashing over the tubes, revealing relatively lower local heat transfer coefficients ranging 6.8–19.6 and 4.5–10.7 kW/m^2 K for upper and lower tubes, respectively.

For the water flow rates of 3, 5 and 7 l/min, the CFD predictions in Fig. 8(b) reveal a nearly symmetric trend of interfacial velocity magnitude between the profiles for the θ ranges of 15°-165° and 195°-345° of the tubes. Firstly, we visualize those high interfacial velocity areas matching the areas with high heat transfer coefficients in essence. At a low water flow rate of 3 l/min, relatively higher interface velocities up to 0.9 m/s are established for $\theta \leq 100°$ and $\theta \geq 260°$ because of the vast majority of water sprays falling on the center region. In contrast, for the studies on falling films [37, 42, 45], the associated interface velocities tend to progressively decline around the tube due to film dispersion, with the formed crests resulting from the accumulation of liquid, indicating the different interfacial velocity profiles of spray films from those of falling films. Overall, the associated interface velocity magnitudes range 0.54−0.88 m/s and 0.35−0.55 m/s around the upper and lower tubes, respectively. Then again, the interfacial velocity profiles at medium and high water flow rates of 5 and 7 l/min resemble the profiles of the tubes at 3 l/min. However, relatively less amounts of liquid splashing around the middle of the tube array can produce lower interfacial velocities varying approximately 0.26–0.70 m/s and 0.22–0.58 m/s for the relevant scenarios of 5 and 7 l/min.

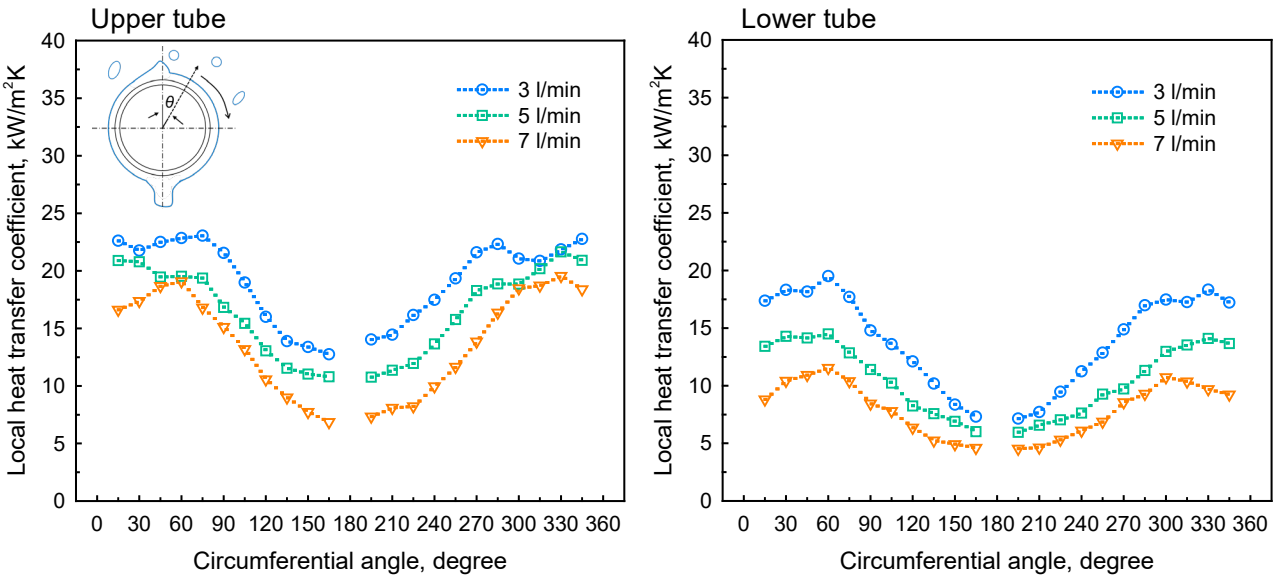

(a)

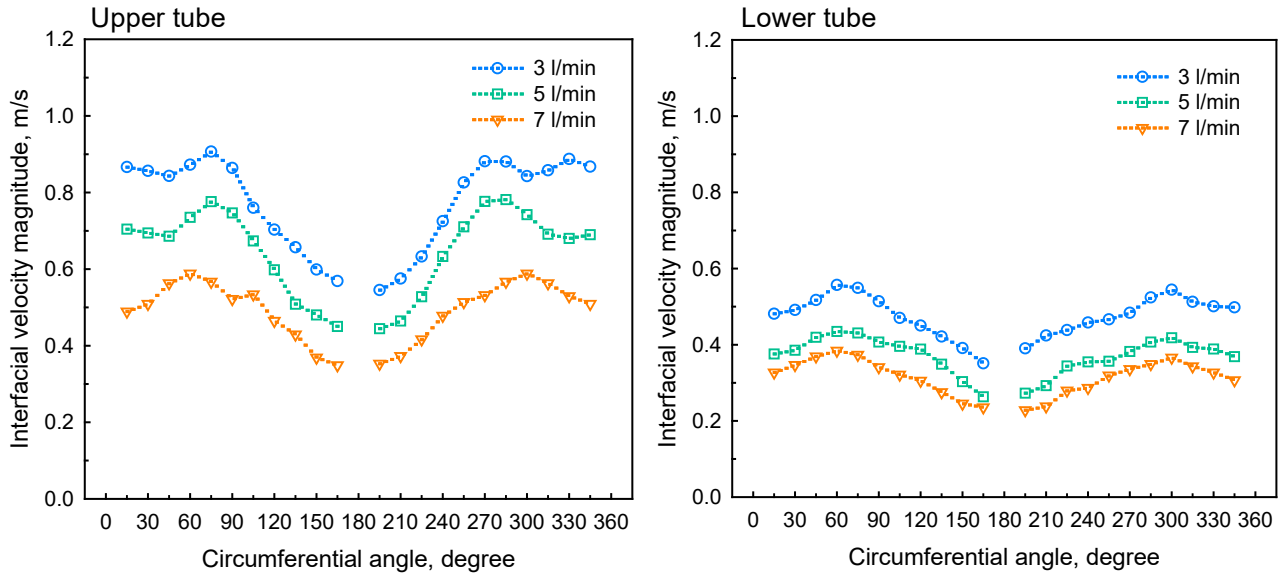

(b)

Fig. 8 Predicted circumferential profiles of (a) heat transfer coefficient and (b) interfacial velocity magnitude in center plane of tubes at w1 position for water flow rates of 3, 5 and 7 l/min

4.2 Effect of tube placement

To explore the tube placement effect on thermal performance, Fig. 9 illustrates the measured average heat transfer coefficients over the outer surfaces of upper and lower tubes at the different positions for a fixed heat flux of 30 kW/m^2 and water flow rates of (a) 3, (b) 5, (c) 7 l/min. The distance in Fig. 9 refers to the horizontal distance of the centerline of the tubes to the baseline (w1). Having the farthest range of water sprays reaching the w3 position (corresponding to a horizontal distance of 57 mm) at 3 l/min, the maximum heat transfer coefficients at the w1 position can

achieve 6.6/5.6 kW/m^{2}K for upper/lower tubes. When the tube placement traveling away from the center line, the thermal outcomes of both test tubes progressively decline to 3.9/2.2 kW/m^{2}K and 2.6/1.6 kW/m^{2}K at the positions of w2 and w3 because of relatively smaller dispersal areas of impinging sprays over the tubes. At a medium water flow rate of 5 l/min, the heat transfer coefficients tend to increase as the positions of tubes are shifted outwards from w1 to w2 and w3. We note the highest heat transfer coefficients of 4.9/4.1 kW/m^{2}K owing to more dropped liquid chunks (from the collisions of liquid sheets with thick rims) splashed over upper/lower tubes at the w3 location. At a horizontal distance of 85.5 mm from the center line, a slight reduction in heat transfer results is noticed in Fig. 9(b) due to the jet-sheet flow mode of water sprays over the tubes at the w4 position. Alternatively, the high momentum flows at 7 l/min tend to produce a larger thin fan-shaped liquid sheet for forming relatively small sprayed water droplets over the tube array with the degraded average heat transfer coefficients of 3.3/2.5 kW/m^{2}K for upper/lower tubes in the middle region (w1). In the meantime, larger-sized liquid blocks splatter on the test tubes at the varied positions from w2 to w5 to achieve the enhanced thermal performance with the peak heat transfer coefficient up to 6.8 kW/m^{2}K for the upper tube. However, it should be noted that the direct impact of liquid jets during sideway falls on the lower tube attains the maximum average heat transfer coefficient of 5.5 kW/m^{2}K at the location of w6 (corresponding to a horizontal distance of 142.5 mm).

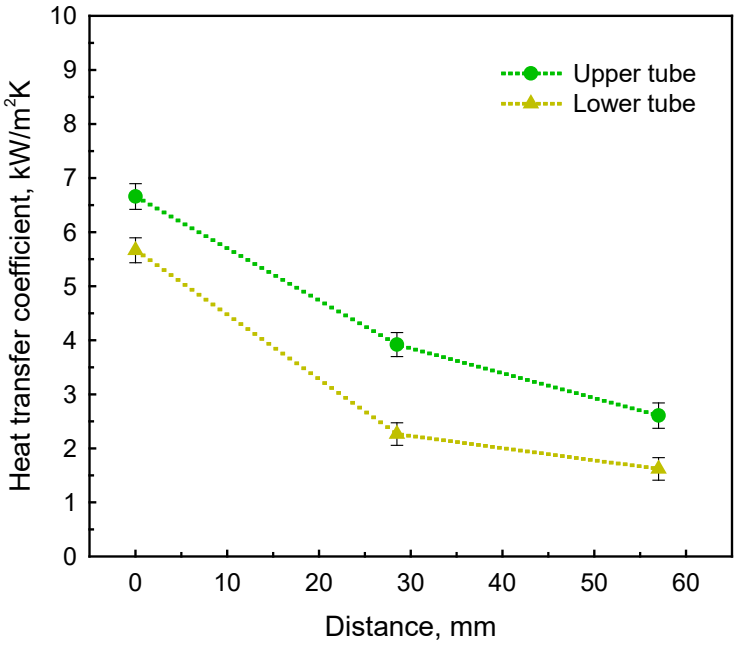

(a)

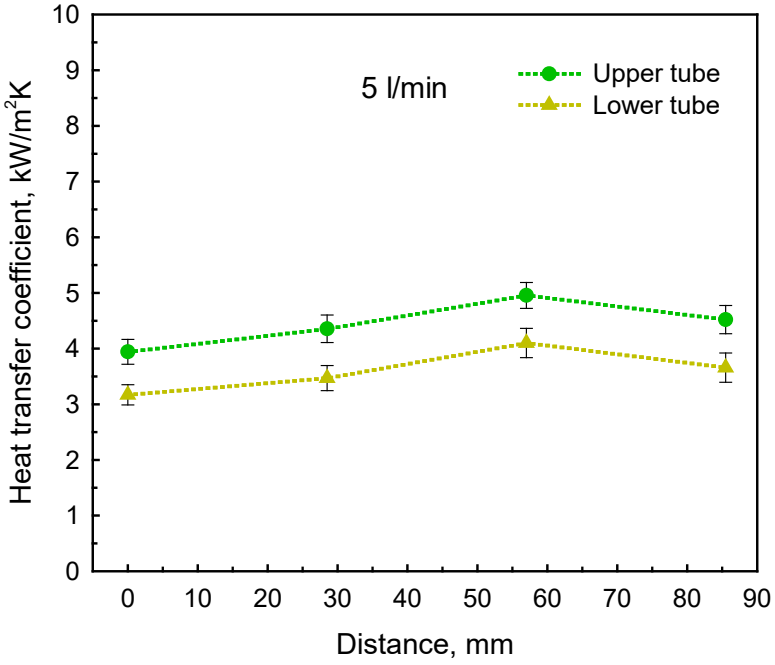

(b)

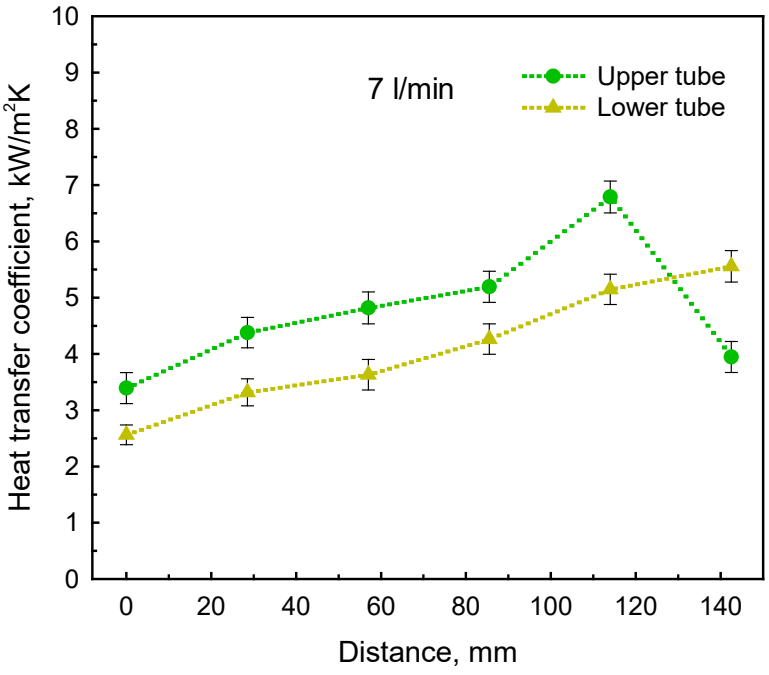

(c)

Fig. 9 Measured average heat transfer coefficients over outer surfaces of upper and lower tubes at varied positions for a fixed heat flux of 30 kW/m^2 and water flow rates of (a) 3, (b) 5, (c) 7 l/min

4.3 Effect of counter current airflow

Considering the water flow rate of 5 l/min at a heat flux of 30 kW/m^{2}K, Fig. 10 illustrates the measured liquid film thickness profiles at the center planes of upper and lower tubes for the counter current velocities (v_{air}) of 0, 0.8, 1.4 and 2.0 m/s, respectively. At v_{air}= 0 m/s, we note relatively thin water films with the thicknesses less than 0.4 mm over both sectors of $\theta \leq 135°$ and $\theta \geq 225°$ of the upper tube. The thicknesses of spray films then accumulate up to 0.6 mm inside the θ ranges of 135°–165°and 195°–225° because of impinged liquid chunks splashing over the tube from diverse directions. In due course, the film thicknesses vary rapidly and congregate at the bottom of the tube (θ= 180°) under gravity. Overall, the associated thicknesses vary from 0.31 mm to 0.59 mm around the upper and lower circular tubes. With the activation of upward airflows, the shear forces impose on the spray films at θ of 135°–165° are relatively stronger than those of 90°–120° to form thicker liquid films with reduced interfacial velocities. Therefore, the thicker liquid films appear over the angle ranges of 90° to 135° for both upper and lower tubes at high airflow velocities of 1.4 and 2.0 m/s. Alternatively, at a low airflow velocity of 0.8 m/s, the thickness of the liquid films range 0.27 mm to 0.50 mm over the upper and lower tubes. The thickness distributions of spray films reveal insignificant differences from those without counter current airflows. It should be noted that the occurrence of liquid accumulation can be still observed at around 150°-165°. In general, the bulk film thickness tends to notably enlarge with increasing upward airflow velocity. The averaged film thicknesses of the upper and lower tubes at v_{air} = 0.8/1.4/2.0 m/s are 3.9%/4.7%/12.1% and 4.3%/ 7.9%/15.6% greater than those at v_{air} = 0 m/s, respectively.

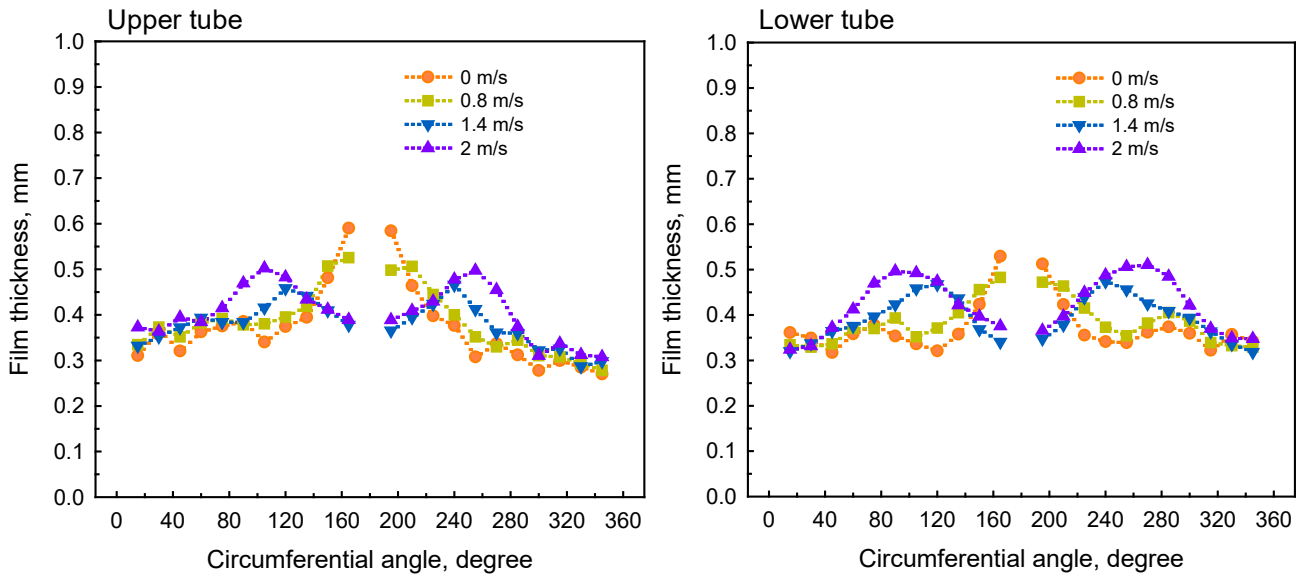

Fig. 10 Measured liquid film thicknesses in center planes of tubes at position w1 for varied counter current airflow velocities with a fixed heat flux of 30 kW/m^2 and a water flow rate of 5 l/min

Fig. 11 illustrates the measured average heat transfer coefficients over the outer surfaces of upper and lower tubes at varied positions and counter current airflow velocities for a fixed heat flux of 30 kW/m^2 and a water flow rate of 5 l/min. Within the test ranges of tube placement position of 85.5 mm (w4) and upward velocity of 2 m/s, the average heat transfer coefficients of upper and lower tubes essentially exhibit an ascending trend with an increase in airflow velocity, indicating stronger cooling outcomes as compared to those without the counter current airflow (v_{air}= 0 m/s). In effect, escalating upward airflow speeds over liquid spray films can produce high shear stresses owing to strong velocity gradients at the film boundaries, and thereby expect to develop steeper temperature gradients at the surface to enhance thermal outcomes [48, 49]. However, the reducing increments of heat transfer coefficient suggest the limitation of thermal performance enhancement by increasing counter current airflow velocity. As reported in prior findings [50, 51], high-speed upward airflows (≥~2.5 m/s) can affect the inter-tube mode transitions and produce an undesirable distribution of falling spray films or even peel off liquid layers to form local dryout, declining the heat and mass transfer performance. Moreover, the heat transfer characteristics with counter current airflows are closely related to the position of tube placement. The upward airflow demonstrates a relatively weaker impact on the outcomes of film thickness and heat transfer of upper tube located in the downwind area than those of lower one. Accordingly, the average heat transfer coefficients (i.e. 4.6/3.8, 4.8/4.0 and 5.0/4.1 kW/m^2 K) of four positions for upper/lower tubes at v_{air}= 0.8, 1.4 and 2.0 m/s are approximately 4.7%/6.5%, 9.2%/12.1% and 11.6%/14.3% greater than those (i.e., 4.4/3.5 kW/m^2 K) without upward airflows.

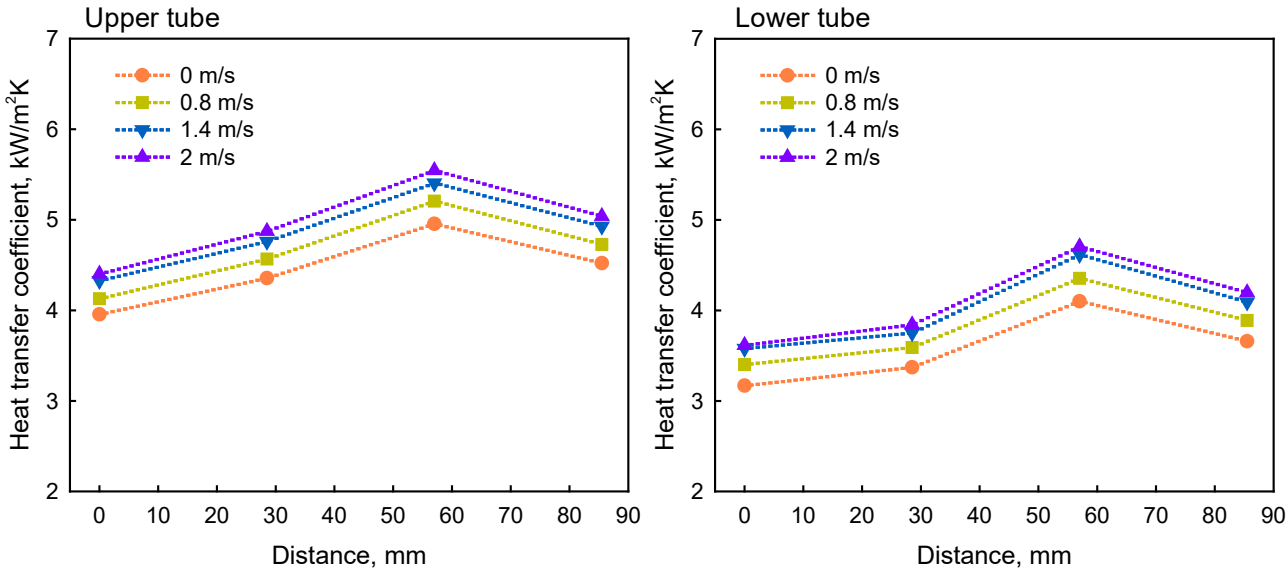

Fig. 11 Measured average heat transfer coefficients over outer surfaces of upper and lower tubes at varied positions and counter current airflow velocities for a fixed heat flux of 30 kW/m^2 and a water flow rate of 5 l/min

5. Conclusions

This study has investigated the evaporative heat transfer progression of falling spray films over the horizontal tube array with counter current airflows by the experimental measurements and 3D unsteady CFD simulations. The main conclusions are summarized below.

(1) The CFD predictions of spray film thickness and thermal outcomes over the tube array agree reasonably with the experimental results. The average deviations of the calculated liquid film thicknesses and heat transfer coefficients with the measurements around the upper and lower tubes are approximately 10.4% and 12.3% as well as 16.3% to 15.7%, respectively.

(2) As compared to the scenario of falling films having the highest thermal performance appeared only on the pinnacle of the tube, the regions of elevated cooling outcomes are broadened due to the multiple impingements of liquid sprays splashed around the tube array. At 3 l/min, we notice several spattered areas with high heat transfer coefficients (up to 20.8 kW/m^2K) over the outer surfaces of upper and lower tubes in the core region. Increasing water flow rates (i.e., 5 and 7 l/min) tend to develop more uniform distributions of high heat transfer coefficients.

(3) Within the water flow rates of 3-7 l/min, the thermal performance is improved with increasing heat fluxes, and the upper tube can provide better cooling outcomes than the lower tube. At 3 l/min, the peak heat transfer coefficients at the central position (w1) are up to 6.6/5.6 kW/m^2K for the upper/lower tubes. As the tubes shifting away from the center line, the associated heat transfer results progressively decline to 3.9/2.2 kW/m^2K and 2.6/1.6 kW/m^2K at the positions of w2 and w3 due to relatively smaller coverage areas of impinging sprays over the tubes. The medium and high water flow rates of 5 and 7 l/min can develop broader spreading extents. The thermal performance tends to increase as the positions of tubes are reallocated outwards with the heat transfer coefficients ranging 3.3-6.8/2.5-5.5 kW/m^2K for upper/lower tubes.

(4) The counter current airflow velocities produce shear forces at the liquid surfaces to form thicker films appearing at θ= 90°-135° for both upper and lower tubes. Specifically, the averaged film thicknesses of the tubes at v_{air} = 0.8-2.0 m/s are 3.9%-15.6% greater than those with no upward airflows.

(5) An increase in counter current airflow velocity effectively enhances the cooling outcomes for falling spray films evaporation on the upper and lower tubes. The upward airflow demonstrates a relatively weaker impact on the outcomes of film thickness and heat transfer of the upper tube than those of lower one located in the windward area. The average heat transfer coefficients (i.e. 4.6/3.8, 4.8/4.0 and 5.0/4.1 kW/m^2K) of four positions for upper/lower tubes at v_{air}= 0.8-2.0 m/s are approximately 4.7%-14.3% greater than those (i.e., 4.4/3.5 kW/m^2K) in a quiescent environment.

Acknowledgment

This study represents part of the results obtained under the support of Ministry of Science and Technology, Taiwan, ROC (Contract No MOST108-3116-F-027-002-CC2, 108-3116-F-027-001 and 110-3116-F-027-001).

References

[1] M. Avgerinou, P. Bertoldi, L. Castellazzi, Trends in data centre energy consumption under the european code of conduct for data centre energy efficiency, Energies, 10(10) (2017) 1470.

[2] Y. Xuan, F. Xiao, X. Niu, X. Huang, S. Wang, Research and application of evaporative cooling in China: A review (I)–Research, Renewable and Sustainable Energy Reviews, 16(5) (2012) 3535-3546.

[3] H.-J. Kim, S.-W. Ham, D.-S. Yoon, J.-W. Jeong, Cooling performance measurement of two cross-flow indirect evaporative coolers in general and regenerative operation modes, Applied Energy, 195 (2017) 268-277.

[4] R.O. Parker, The Heat-Mass-Transfer Characteristics of AN Evaporative Cooler, Ph. D. Thesis, (1959).

[5] T. Mizushima, R. Ito, H. Miyashita, Experimental study of an evaporative cooler, International chemical engineering, 7(4) (1967) 727-+.

[6] A. Dreyer, P. Erens, Heat and mass transfer coefficient and pressure drop correlations for a crossflow evaporative cooler, in: Proceedings of the Ninth International Heat Transfer Conference, Hemisphere Publ. Co New York, USA, 1990, pp. 233-238.

[7] Y. Niitsu, K. Naito, T. Anzai, Studies on characteristics and design procedure of evaporative coolers, Journal of SHASE, Japan, 43(7) (1969) 581-590.

[8] A. Hasan, K. Siren, Performance investigation of plain and finned tube evaporatively cooled heat exchangers, Applied thermal engineering, 23(3) (2003) 325-340.

[9] H.M. Ettouney, H.T. El-Dessouky, W. Bouhamra, B. Al-Azmi, Performance of evaporative condensers, Heat Transfer Engineering, 22(4) (2001) 41-55.

[10] M. Hosoz, A. Kilicarslan, Performance evaluations of refrigeration systems with air‐cooled, water‐cooled and evaporative condensers, International journal of energy research, 28(8) (2004) 683-696.

[11] E. Hajidavalloo, H. Eghtedari, Performance improvement of air-cooled refrigeration system by using evaporatively cooled air condenser, International journal of refrigeration, 33(5) (2010) 982-988.

[12] J. Heyns, D. Kröger, Experimental investigation into the thermal-flow performance characteristics of an evaporative cooler, Applied Thermal Engineering, 30(5) (2010) 492-498.

[13] I. Finlay, D. Harris, Evaporative cooling of tube banks, International journal of refrigeration, 7(4) (1984) 214-224.
[14] M. Islam, K. Jahangeer, K. Chua, Experimental and numerical study of an evaporatively-cooled condenser of air-conditioning systems, Energy, 87 (2015) 390-399.
[15] A.Y.T. Al-Zubaydi, G. Hong, Experimental study of a novel water-spraying configuration in indirect evaporative cooling, Applied Thermal Engineering, 151 (2019) 283-293.
[16] G.B. Hill, E. Pring, P.D. Osborn, Cooling towers: principles and practice, Butterworth-Heinemann, 2013.
[17] S. De Antonellis, C.M. Joppolo, P. Liberati, S. Milani, L. Molinaroli, Experimental analysis of a cross flow indirect evaporative cooling system, Energy and Buildings, 121 (2016) 130-138.
[18] L.-H. Chien, J.-J. Xu, T.-F. Yang, W.-M. Yan, Experimental study on water spray uniformity in an evaporative condenser of a water chiller, Case Studies in Thermal Engineering, 15 (2019) 100512.
[19] G. Moreno Jr, S.M. You, E. Steinthorsson, Spray cooling performance of single and multi-jet spray nozzles using subcooled FC-72, in: Heat Transfer Summer Conference, 2007, pp. 783-790.
[20] S. Nižetić, D. Čoko, A. Yadav, F. Grubišić-Čabo, Water spray cooling technique applied on a photovoltaic panel: The performance response, Energy conversion and management, 108 (2016) 287-296.
[21] R. Payri, F.J. Salvador, J. De la Morena, V. Pagano, Experimental investigation of the effect of orifices inclination angle in multihole diesel injector nozzles. Part 2–Spray characteristics, Fuel, 213 (2018) 215-221.
[22] Y.-T. Lee, S. Hong, L.-H. Chien, W.-H. Lin, A.-S. Yang, Liquid film dispersion on horizontal circular tubes under spray impingement, International Journal of Heat and Mass Transfer, 160 (2020) 120223.
[23] X. Zhu, S. Chen, S. Shen, S. Ni, X. Shi, Q. Qiu, Experimental study on the heat and mass transfer characteristics of air-water two-phase flow in an evaporative condenser with a horizontal elliptical tube bundle, Applied Thermal Engineering, 168 (2020) 114825.
[24] W.-M. Yan, C.-W. Pan, T.-F. Yang, M. Ghalambaz, Experimental study on fluid flow and heat transfer characteristics of falling film over tube bundle, International Journal of Heat and Mass Transfer, 130 (2019) 9-24.
[25] M. Može, M. Zupančič, I. Golobič, Investigation of the scatter in reported pool boiling CHF measurements including analysis of heat flux and measurement uncertainty evaluation methodology, Applied Thermal Engineering, 169 (2020) 114938.
[26] S. Hong, B. Zhang, C. Dang, E. Hihara, Development of two-phase flow microchannel heat sink applied to solar-tracking high-concentration photovoltaic thermal hybrid system, Energy, 212 (2020) 118739.
[27] J.U. Brackbill, D.B. Kothe, C. Zemach, A continuum method for modeling surface tension, Journal of computational physics, 100(2) (1992) 335-354.

[28] E. Delnoij, J. Kuipers, W.P.M. van Swaaij, Computational fluid dynamics applied to gas-liquid contactors, Chemical Engineering Science, 52(21-22) (1997) 3623-3638.
[29] D. Gueyffier, J. Li, A. Nadim, R. Scardovelli, S. Zaleski, Volume-of-fluid interface tracking with smoothed surface stress methods for three-dimensional flows, Journal of Computational physics, 152(2) (1999) 423-456.
[30] M. Meier, G. Yadigaroglu, B.L. Smith, A novel technique for including surface tension in PLIC-VOF methods, European Journal of Mechanics-B/Fluids, 21(1) (2002) 61-73.
[31] Z. Yang, X. Peng, P. Ye, Numerical and experimental investigation of two phase flow during boiling in a coiled tube, International Journal of Heat and Mass Transfer, 51(5-6) (2008) 1003-1016.
[32] Z. Wang, S. Li, R. Chen, X. Zhu, Q. Liao, Simulation on the dynamic flow and heat and mass transfer of a liquid column induced by the IR laser photothermal effect actuated evaporation in a microchannel, International Journal of Heat and Mass Transfer, 113 (2017) 975-983.
[33] R. Marek, J. Straub, Analysis of the evaporation coefficient and the condensation coefficient of water, International Journal of Heat and Mass Transfer, 44(1) (2001) 39-53.
[34] M. Bond, H. Struchtrup, Mean evaporation and condensation coefficients based on energy dependent condensation probability, Physical Review E, 70(6) (2004) 061605.
[35] C.R. Kharangate, H. Lee, I. Mudawar, Computational modeling of turbulent evaporating falling films, International Journal of Heat and Mass Transfer, 81 (2015) 52-62.
[36] Y. Zhou, Z. Cai, Z. Ning, M. Bi, Numerical simulation of double-phase coupled heat transfer process of horizontal-tube falling film evaporation, Applied Thermal Engineering, 118 (2017) 33-40.
[37] Y.-T. Lee, S. Hong, C. Dang, L.-H. Chien, L.-W. Chang, A.-S. Yang, Heat transfer characteristics of obliquely dispensed evaporating falling films on an elliptic tube, International Journal of Heat and Mass Transfer, 132 (2019) 238-248.
[38] M. Woelke, Eddy viscosity turbulence models emploed by computational fluid dynamic, Prace Instytutu Lotnictwa, (2007) 92-113.
[39] Y. Suzen, G. Xiong, P. Huang, Predictions of transitional flows in low-pressure turbines using intermittency transport equation, AIAA journal, 40(2) (2002) 254-266.
[40] A.F. ANSYS, version 14.0: user manual, ANSYS, Inc., Canonsburg, USA, (2011).
[41] D. Jang, R. Jetli, S. Acharya, Comparison of the PISO, SIMPLER, and SIMPLEC algorithms for the treatment of the pressure-velocity coupling in steady flow problems, Numerical Heat Transfer, Part A: Applications, 10(3) (1986) 209-228.
[42] C.-Y. Zhao, W.-T. Ji, Y.-L. He, Y.-J. Zhong, W.-Q. Tao, A comprehensive numerical study on the subcooled falling film heat transfer on a horizontal smooth tube, International Journal of Heat and Mass Transfer, 119 (2018) 259-270.
[43] H. Ding, P. Xie, D. Ingham, L. Ma, M. Pourkashanian, Flow behaviour of drop and jet modes of a laminar falling film on horizontal tubes, International Journal of Heat and Mass Transfer, 124

(2018) 929-942.
[44] Q. Qiu, X. Zhang, S. Quan, X. Zhu, S. Shen, 3D numerical study of the liquid film distribution on the surface of a horizontal-tube falling-film evaporator, International Journal of Heat and Mass Transfer, 124 (2018) 943-952.
[45] Z. Wan, Y. Li, S. Wang, A comprehensive simulation and optimization on heat transfer characteristics of subcooled seawater falling film around elliptical tubes, Applied Thermal Engineering, 189 (2021) 116675.
[46] Y.-T. Lee, S. Hong, C. Dang, L.-H. Chien, A.-S. Yang, Effect of counter current airflow on film dispersion and heat transfer of evaporative falling film over a horizontal elliptical tube, International Journal of Heat and Mass Transfer, 141 (2019) 964-973.
[47] F. Tahir, A. Mabrouk, M. Koc, Influence of co-current vapor flow on falling film over horizontal tube, International Journal of Thermal Sciences, 159 (2021) 106614.
[48] M. Fiorentino, G. Starace, The design of countercurrent evaporative condensers with the hybrid method, Applied Thermal Engineering, 130 (2018) 889-898.
[49] C.-Y. Zhao, W.-T. Ji, P.-H. Jin, S. Yoshioka, W.-Q. Tao, Effect of downward vapor stream on falling film evaporation of R134a in a tube bundle, International Journal of Refrigeration, 89 (2018) 112-121.
[50] B. Ruan, A.M. Jacobi, L. Li, Effects of a countercurrent gas flow on falling-film mode transitions between horizontal tubes, Experimental thermal and fluid science, 33(8) (2009) 1216-1225.
[51] W.-T. Ji, C.-Y. Zhao, D.-C. Zhang, S. Yoshioka, Y.-L. He, W.-Q. Tao, Effect of vapor flow on the falling film evaporation of R134a outside a horizontal tube bundle, International Journal of Heat and Mass Transfer, 92 (2016) 1171-1181.

Nomenclature

d	Outer diameter of the test tube
F_σ	Surface tension force at the liquid-gas interface
g	Gravitational acceleration
H	Height
h_{ave}	Average heat transfer coefficient
L	Effective heated length of the tube
p	Pressure
Q	Total heat generated in the heating rod

q_{eff}	Effective heat flux
Re	Film Reynolds number
$T_{w,\,ave}$	Average wall temperature
T_o	Average outlet temperature of spray nozzles
t	Time
$\vec{V}$	Velocity vector
W	Wide
α	Volumetric fraction of liquid phase
κ	Surface curvature
Γ	Mass flow rate per unit length
δ	Film thickness
θ	Circumferential angle
ρ	Density
ρ_w	Density of the water
ρ_a	Density of the air
μ_{eff}	Effective viscosity
μ_w	Viscosity of the water
μ_a	Viscosity of the air
σ	Surface tension